The development and characterization of electroless Ni-P nanocomposite coatings and investigation of their corrosion resistance

by

Shuo Shuang

A thesis submitted in partial fulfillment of the requirements for the degree of

Master of Science

in

Chemical Engineering

The Department of Chemical and Materials Engineering
University of Alberta

Abstract

The Steam Assisted Gravity Drainage (SAGD) system is a commonly empolyed method to extract crude oil in Alberta. The slotted liners of the SAGD system are made of L80 carbon steel, which is prone to the corrosion attack in the corrosive serving environment containing H_2S and CO_2. To reduce the corrosion rate and extend the lifetime of slotted liners, an electroless deposition of nickel–phosphorous (Ni-P) coating is applied on the carbon steel. Ni-P coating has unique properties such as remarkably high hardness, wear resistance and exceptional corrosion resistance. However, there are still some intrinsic defects in the Ni-P matrix, which enables aggressive ions to reach the substrate. It should be noted that nanoparticles possess many well-known physical and chemical properties because of their quantum size effect. Therefore, developing Ni-P nanocomposite coating is an effective strategy to modify the physicochemical property of the Ni-P coating.

The goal of this study was to develop Ni-P nanocomposite coatings by adding nanoparticles to the plating solution, thereby filling defects in the Ni-P coating with nanoparticles and improving the performance of the Ni-P coating.

The Ni-P-WC and Ni-P-Fe_3O_4 coatings were prepared by electroless deposition methods, modifying the typical Ni–P coating by adding of different amounts of WC and Fe_3O_4 nanoparticles, respectively. The morphology, structure, microhardness, and corrosion resistance of the Ni-P-WC coating, Ni-P-Fe_3O_4 coating, and conventional Ni-P coating were analyzed using optical stereoscopic microscopy (OSM), scanning electron microscopy (SEM), polarization curve and electrochemical impedance spectroscopy (EIS), X-ray powder diffraction (XRD) and Vickers hardness tests.

The study showed that WC nanoparticles had an important impact on the microhardness, anti-corrosion properties and morphology of the coatings. The results of electrochemical tests in the National Association of Corrosion Engineers (NACE) standard solution containing CO_2 and H_2S showed that the electroless Ni-P-WC coating exhibited better anti-corrosion ability than the Ni-P coating. The superior stability of the Ni-P-WC coating was confirmed by long-term immersion tests in the simulated solution. The Ni-P-WC coating also had an increased hardness than the Ni-P coating. The coating formed in the bath containing 5 g/L WC particles showed the highest hardness value and best corrosion resistance.

The results showed that Fe_3O_4 nanoparticles deposited homogeneously on the Ni-P matrix. The electroless nanocomposite coatings exhibited an amorphous structure. The results of corrosion tests in the 3.5 wt. % NaCl solution indicated that the electroless Ni-P-Fe_3O_4 coating proved to be much more corrosion resistant than the conventional Ni–P electroless coating. With Fe_3O_4 concentrations were increased from 0 g/L to 3.0 g/L in the plating solution, the corrosion resistance of Ni-P-Fe_3O_4 coating increased and then decreased. This increasing-and-decreasing tendency was also observed in thickness of the coating. The coating demonstrated the best corrosion resistance and maximum thickness when the concentration of Fe_3O_4 was 0.8 g/L in the plating solution. In immersion tests, the Ni-P-Fe_3O_4 coating showed better stability than the Ni-P coating.

Correspondingly, the rational mechanism behind the improvement of corrosion resistance due to the addition of Fe_3O_4 was further discussed.

Preface

This thesis is an original work by Shuo Shuang. No part of this thesis has been previously published as journal articles, books and conference papers.

Acknowledgements

Firstly, I would like to express my sincere and absolute gratitude to my supervisors, Dr. Jing-Li Luo and Dr. Hongbo Zeng for their numerous patient guidance, kind assistance, tremendous support and encouragement in my two-year study. They provided me with help not only on the scientific research but also on my career development and personal life.

Next, my deep appreciations go to Dr. Chong Sun for his meaningful suggestions on my experimental design, data analysis, and academic writings. I also acknowledge Yaqian Zhang and Dr. Subiao Liu for their insightful advice on my research. I also would like to thank Jiankuan Li for his valuable discussions.

Then, I am grateful to my group members Xianzong Wang, Kaiyang Li, Minkang Liu, Tengfei Li, Yuanyuan Hong, Jing Xiao, Shaochen Ding, Dr. Meng Li, Dr. Bin Hua, Shawn Zhang, Minrui Gao for establishing such a great work atmosphere.

This work would not have been completed without the financial support of RGL Inc. and NSERC.

Finally, my deepest gratitude goes to my parents, Shigang Liu and Xiaojun Liang, for their constant love and encouragement.

Table of Contents

List of Figures

List of Tables

List of Abbreviations

SAGD	Steam Assisted Gravity Drainage
Ni–P	Nickel–Phosphorous
VCL	Volatile Corrosion Inhibitor
ICCP	Impressed Current Cathodic Protection
SDS	Sodium Dodecyl Sulfate
WE	Working Electrode
CE	Counter Electrode
RE	Reference Electrode
EIS	Electrochemical Impedance Spectroscopy
AC	Alternative Current
OSM	Optical Stereoscopic Microscope
SEM	Scanning Electron Microscope
SE	Secondary Electrons
BSE	Back-Scattered Electrons
EDS	Energy-Dispersive X-ray Spectroscopy
XRD	X-ray diffraction
OCP	Open-Circuit Potential
SCE	Saturated Calomel Electrode

Glossary of Terms

Z	Impedance, Ω
Z_{real}	The real part of impedance, Ω
Z_{imag}	The imaginary part of impedance, Ω
F	Weight load, kgf
d	Average of two diagonals caused by the indenter, mm
E_{corr}	Corrosion potential, V
I_{corr}	Corrosion current, A cm^{-2}
R_s	Resistance of the solution, Ω cm^2
R_{coat}	Resistance of the coating, Ω cm^2
R_{ct}	Charge transfer resistance, Ω cm^2
R_p	Sum of coating resistance and charge transfer resistance, Ω cm^2
CPE_1	Coating capacitance, Ω^{-1} cm^{-2} s^{-n}
CPE_2	Capacitance of the double layer, Ω^{-1} cm^{-2} s^{-n}

1. Introduction

1.1 Steam Assisted Gravity Drainage systems

Oil and gas resources in Alberta play a central role in the Canadian petroleum industry, supplying not only reliable and stable energy to the world but also making a significant contribution to the Canadian economy. Alberta's oil sands are the third-largest proven crude oil reserve in the world, next to those in Saudi Arabia and Venezuela. The crude bitumen production was as high as 2.5 million barrels per day in 2016 [1]. The main resource for oil production in Alberta is the oil sands, which consist of a mixture of bitumen, water, sand, and clay [2]. Most reserves can only be recovered by in-situ methods, rather than surface mining [3].

One of the essential in-situ methods is the Steam Assisted Gravity Drainage (SAGD) system (Figure 1.1), which can pump up the oil sand deposits in the deep position to the ground and enhance oil recovery. At room temperature, the viscosity of bitumen is such high, prohibiting the flow of bitumen. The basic working principle of SAGD is to heat up the upper region of the reserve to reduce the viscosity of oil so that it drains to the lower region under gravity, after which oil is transported to the ground and stored for further treatment.

In the SAGD process, there are two parallel horizontal wellbores, one over the other. The upper wellbores are used to inject high-pressure steam, while the lower wellbores are responsible for collecting heated bitumen and pumping it up to the ground.

A significant component of the SAGD system is the slotted liners (Figure 1.1): Very slender slots perforate a liner pipe which allows steam to exit along the injection wellbore and filter sands from the oil entering the collection wellbore.

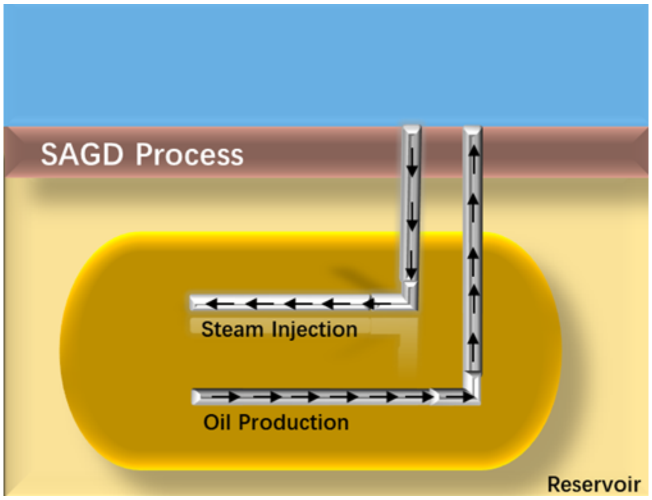

Figure 1.1 Steam-assisted gravity drainage system and slotted liner [1].

However, the presence of different corrosive agents which are either in the reserves or are generated in the oil recovery process can and does lead to extremely severe service conditions. Corrosion reduces the life of the equipment, such as slotted liners in SAGD, decreasing production efficiencies and increasing production costs. Corrosion also has a negative effect on production safety and the environment.

To tackle those corrosion problems, the Faculty of Engineering at the University of Alberta is collaborating with RGL Reservoir Management Inc., a leading supplier of completion tools for enhanced oil recovery. The primary objective of the project is to improve the service life of slotted liner by enhancing the corrosion resistance of carbon steels used for slotted liners, thus increasing overall productivity. This objective is accomplished by developing a corrosion resistant coating.

1.2 Corrosion related problems of the slotted liners

Extremely corrosive substances such as CO_2, H_2S and chlorine ions in underground fluids aggravate the corrosion process [3,4]. The major corrosion processes occurring on the slotted liner of SAGD systems consist of sweet corrosion (CO_2 corrosion), sour corrosion (H_2S corrosion), CO_2/H_2S synergism corrosion, sulfide stress cracking (SSC) and erosion corrosion [5].

A certain level of CO_2 in the oil and gas production wells induces sweet corrosion. The electrochemical reaction between CO_2 and carbon steel can form a corrosion product layer of $FeCO_3$ on the surface of carbon steel. This layer can either protect the carbon steel by blocking the corrosive media or break under the influence of flowing fluids, highly depending on environmental conditions such as pH and temperature. The corrosion that occurs when metal degrades after contacting with H_2S and moisture is sour corrosion. H_2S can act in two means: (1) dissolved H_2S in aqueous solutions produces hydrogen ions, which increase the corrosion rate. (2) H_2S acts as a hydrogen recombination poison, facilitating the diffusion of atomic hydrogen into steel. The volume of the corrosion product (iron sulfides) is much larger than that of corroded carbon steel, clogging the slots and hindering oil transportation. Another corrosion product, hydrogen, is harmful to the mechanical strength of carbon steel.

The relative motion between the metal surface and a corrosive fluid induces erosion corrosion.

Erosion corrosion results from both electrochemical corrosion and mechanical erosion. When combines, these forms of corrosion accelerate the rate of material deterioration and cause much more severe damage to the material.

1.3 Electroless Ni-P coating

Various corrosion protection techniques such as cathodic protection and inhibitors have been developed to alleviate the corrosion, but for slotted liners protective coatings are more economical and environmentally friendly.

Applying coatings is a preferred approach to surface protection, and it is widely used in oil-and-gas production. Many studies have focus on the synthesis of coatings, including coatings based on Cr [6], Zn-Mg [7], Zn-Mg-Al [8], Ti-Al [9], the Co matrix [10] and the Ni-P matrix [11]. Among these coatings, the electroless Ni-P coating is a well-known surface modification process, which has received widespread acceptance in the industry due to its low costs and high resistance to corrosion [12].

Despite the good performance of electroless Ni-P coating, the coating still has defects such as pores and dislocations in its structure. The properties of Ni-P coating can be further enhanced by modification methods to meet different demands and prolong the lifetime of coatings in specific environments. For example, the co-deposition of metal elements including Cu, and Zu can improve corrosion resistance and mechanical properties [13, 14]. Another effective method to tailor the properties of Ni-P coating is to incorporate nanoparticles in the Ni-P matrix [15].

As a type of hard particles, carbon tungsten (WC) has been used in many fields such as catalysts in chemical and electrochemical reactions [16]. Although there is some literature about Ni-P-WC coatings [17], most studies have focused on how erosion resistance and mechanical properties were improved via the co-deposition of WC nanoparticles. Few systematic studies have looked at how the WC influences the corrosion resistance of coatings in an oil production environment that contain H_2S and CO_2.

There is limited literature on the incorporation of Fe_3O_4 nanoparticles in the synthesis of Ni-P based coating, despite the advantages such as low costs and abundance. The Fe_3O_4 nanoparticle is also a decent candidate for Ni-P nanocomposite coatings.

1.4 Objectives

Based on the limited service life of Ni-P coating in the oil sand environment that contains CO_2 and H_2S, it is imperative to develop an innovative coating to enhance the corrosion resistance of Ni-P coating. Two kinds of electroless Ni-P nanocomposite coatings are proposed for development and investigation: Ni-P-WC and Ni-P-Fe_3O_4. The study is about the fabrication of coatings made from Ni-P-WC and Ni-P-Fe_3O_4, and about the investigation into the performance of these two nanocomposite coatings.

(1) The first objective of my work is to is to incorporate WC nanoparticles into the Ni-P coating. I will then investigate the effect of WC nanoparticles on the morphology, hardness and anti-corrosion properties of the Ni-P based coatings.

(2) Another goal is to prepare Ni-P-Fe_3O_4 coatings by electroless deposition. I will study the morphology, chemical composition, thickness, structure, corrosion resistance and stability of the Ni-P-Fe_3O_4 coatings and compare them with the Ni-P coating.

(3) Both the Ni-P-WC and Ni-P-Fe_3O_4 coatings will be synthesized with different concentrations of nanoparticles in the plating bath. The third objective is to study the effect of the nanoparticle concentration on the properties of the Ni-P nanocomposite coatings.

1.5 Thesis contents

As shown in Figure 1.2, Chapter 2 will review the literature related to corrosion environments, Ni-P coatings, and Ni-P nanocomposite coatings. The methodology used in the experimental procedures will be described in Chapter 3. Chapter 4 and Chapter 5 will describe and discuss the results of the Ni-P-WC coating and Ni-P-Fe_3O_4 coating, respectively. Chapters 7 and 8 are about general conclusions and future work, respectively.

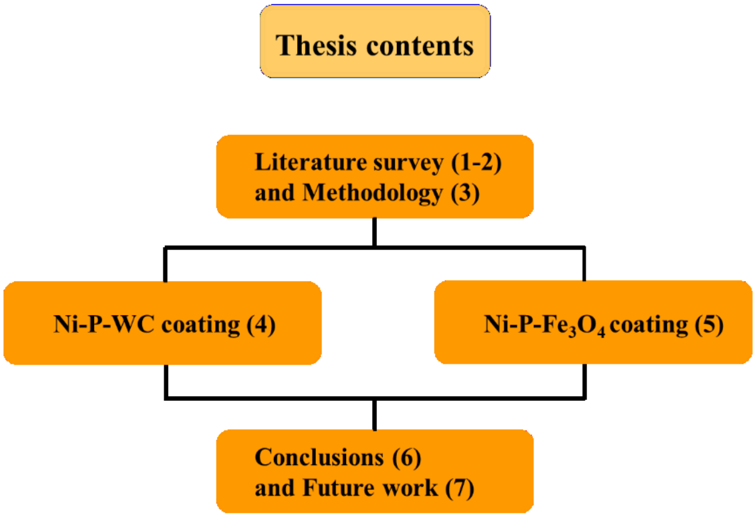

Figure 1.2 Main contents of the thesis.

2. Literature review

2.1 The corrosion environments

2.1.1 Corrosive gases

To deal with the high viscosity of bitumen at room temperature, a variety of methods has been employed to increase the recovery efficiency and enhance bitumen production [18]. The Steam Assisted Gravity Drainage (SAGD) process is a widely used strategy for producing bitumen out of oil sands. As mentioned before in Chapter 1, the bitumen is heated by the saturated steam to above 180°C.

However, at such high temperature, acid gases such as CO_2, and H_2S are generated from the aquathermolysis process, which is a chemical reaction involving the application of high-temperature high-pressure steam to break bonds (e.g., the C-S bond) in resins and asphaltenes [19]. The chemical composition of the produced gas is approximately 15% CO_2 and 0.6% H_2S when the temperatures is 180°C. The generation rate of these gases is strongly influenced by operating conditions, especially the steam temperature. A higher temperature can produce more CO_2 and H_2S gases.

It should be pointed out that the pH of the aqueous phase in SAGD is essentially influenced by the dissolution of CO_2 and H_2S. The acidic environment will lead to more serious corrosion compared with the neutral or alkaline environment. The harmful effect of CO_2 and H_2S on the service time of slotted liners has been discussed by a large number of researchers [3-6].

The corrosion rate of carbon steel in simulated SAGD produced fluids was predicted by Case et al. [20] through thermodynamic modeling. The results indicated that the corrosion rate was very low due to the adherent protective layers of Fe_2O_3/Fe_3O_4 which formed on the substrate surface, and that these layers could extend the service life of the liners to and beyond 50 years. Moreover, the formation of these protective layers was enhanced by high temperatures, which reduced CO_2 and H_2S gas solubility in produced water.

Whittaker et al. [21] argued that severe corrosion and failure occurred on piping, elbows, tees and reducers in the SAGD process after only five years of service. The general corrosion rates were as high as eight mm/year. The main corrosion product, $FeCO_3$, could be removed from the metal surface under turbulent flow. As a result, stable protective layers would fail to form, leaving the carbon steel constantly exposed to corrosive media. The significant difference between Case and Whittaker was a result of the influence of the fluids' velocity. The model used by Case et al. only considered thermodynamic equilibrium, while Whittaker et al. pointed out that the CO_2/impingement corrosion is the main cause of failures. Dugstad et al. [22] stated that the corrosion rate in the CO_2 corrosion process could be increased from three mm/y to thirty-three mm/y when the water flow velocity increased from zero to one m/s. Field data from Whittaker et al. is more credible.

The high corrosion rate of carbon steel caused by CO_2/H_2S in the SAGD system indicates the great need to develop protective methods to prevent corrosion in pipelines.

2.1.2 Corrosive ions and solid particles

Another reason that steel pipelines in the SAGD system suffer from erosion-corrosion is because of an aqueous solution containing corrosive ions such as Na^+, Ca^{2+}, Mg^{2+} Cl^-, HCO_3^-, SO_4^{2-}, and solid particles such as silica sand and clay [23,24]. A wide variation of ion concentrations was detected by Liu et al. [25], which can be explained by different oil reserves and different amounts of in-situ water carried by condensed steam. Some of these ions have a detrimental impact on corrosion behaviors of steel liners. For example, Cl^- could destroy the corrosion product film and increase the corrosion rate [26]. Also, the impingement of fluids with a high content of solid particles can cause erosion by destroying the corrosion product scale and causing plastic deformation [27]. The synergistic attack of erosion and corrosion can lead to much greater weight loss of pipelines. Thus, the mechanical properties like hardness should also be regarded as an essential factor in the selection of protective methods.

2.1.3 Line pipe material

Although carbon steels have weaknesses such as worse anti-corrosion properties compared to stainless steel, they are commonly used in oil and gas production because of their evident advantages such as fabricability, availability and relatively low costs. L80 carbon steel was selected as the substrate in this study because it is the material employed in slotted liners [28].

2.2 The corrosion mechanism

The corrosion mechanisms of carbon steel in the field are complicated due to the complex compositions of corrosive media. Two typical corrosion mechanisms will be briefly discussed in this section.

2.2.1 Sweet corrosion

CO_2 corrosion, also known as "sweet corrosion," has been recognized as the most prevalent form of corrosion occurring on carbon steel liners in the oil filed [29]. The dry CO_2 gas itself is not corrosive in the temperature range of oil and gas production. However, dissolved CO_2 can change the pH of the aqueous phase, promoting the electrochemical reaction between the carbon steel and the corrosive solution. Severe localized corrosion can result from the presence of CO_2 in the aqueous phase.

Various parameters such as temperature, pH, CO_2 partial pressure, and fluid dynamics are interdependent and form an important part of the CO_2 corrosion mechanism. Different mechanisms of CO_2 corrosion in diverse conditions have been proposed by researchers [30,31]. A general corrosion process will be discussed below. The initiating step is the formation of a weak acid (H_2CO_3) [30].

$$\mathrm{CO_2 + H_2O \leftrightarrow H_2CO_3} \qquad (2\text{-}1)$$

Carbon acid can dissociate [31],

$$H_2CO_3 \leftrightarrow H^+ + HCO_3^- \qquad (2\text{-}2)$$

$$HCO_3^- \leftrightarrow H^+ + CO_3^{2-} \qquad (2\text{-}3)$$

There are three cathodic reactions including the reduction of carbon acid and bicarbonate ions,

$$2H_2CO_3 + 2e^- \leftrightarrow H_2 + 2HCO_3^- \qquad (2\text{-}4)$$

$$2HCO_3^- + 2e^- \leftrightarrow H_2 + 2CO_3^{2-} \qquad (2\text{-}5)$$

and the reduction of hydrogen ions,

$$2H^+ + 2e^- \leftrightarrow H_2 \qquad (2\text{-}6)$$

The anodic reaction occurs by the oxidation of iron,

$$Fe + 2e^- \leftrightarrow Fe^{2+} \qquad (2\text{-}7)$$

These ions can contribute to the formation of iron carbonate ($FeCO_3$),

$$Fe^{2+} + CO_3^{2-} \leftrightarrow FeCO_3 \qquad (2\text{-}8)$$

$$Fe^{2+} + 2HCO_3^- \leftrightarrow Fe(HCO_3)_2 \qquad (2\text{-}9)$$

$$Fe(HCO_3)_2 \leftrightarrow FeCO_3 + CO_2 + H_2O \qquad (2\text{-}10)$$

CO_2 corrosion of carbon steel highly depends on the corrosion product films formed on the surface during the corrosion process. It is noteworthy that the films containing the same components can be either corrosive or protective [31]. Anti-corrosion properties are not influenced by the thickness of films, but by the morphology and structure. The films should be adherent, fully covering the surface to achieve successful protection.

Temperature plays an important role in the growth of the films by influencing iron carbonate solubility [32]. Films can be divided into four classes in different ranges of temperature: transparent, iron carbide (Fe_3C), iron carbonate ($FeCO_3$), and magnetite (Fe_3O_4). Researchers rarely study the transparent film, and its main composition is iron and oxygen. Despite its anti-corrosion properties, this film is <1 μm thick and can be detected only at and below room temperature.

When the temperature is low (< 60 °C), the solubility of iron carbonate in water is high, resulting in the low growth rate of $FeCO_3$ film. The main chemical constitution of the film is cementite (Fe_3C), which is fragile and porous. Thus, this kind of film is unstable and brittle under the attack of flowing fluids. Moreover, this film can even aggravate the corrosion process by promoting galvanic corrosion and causing local acidification.

Above 60°C, the protectiveness of the film increases with the rising temperature because of the decreasing solubility of iron carbonate. These adherent $FeCO_3$ scales prevent the corrosion process and limit the electrochemical activity by covering the defects of carbon steel and reducing the contacting area between carbon steel and corrosive media. When the temperature reaches 100°C, magnetite (Fe_3O_4) tends to form a stable scale.

The environmental pH is also essential to the carbon steel ‘s CO_2 corrosion rate, because the corrosion rate is influenced by ion concentrations. This, further affects the electrochemical reactions [33]. The lower pH represents a higher concentration of H^+, which can initiate and accelerate the localized corrosion. In contrast, the increasing pH can slow the reduction of hydrogen ions, which further decreases the ion's anodic oxidation rate. A higher pH can also reduce the solubility of iron carbonate in water, promoting the precipitation of the protective scale and decreasing the corrosion rate of carbon steel.

2.2.2 Sour corrosion

Hydrogen sulfide corrosion (sour corrosion) is another major type of corrosion. Sulfide stress corrosion cracking, hydrogen-induced cracking, and hydrogen sulfide corrosion have been discussed extensively because a high concentration of H_2S can result in localized corrosion and cause construction materials to fail in the oil and gas industry [34]. The mechanism of H_2S corrosion is complex and not well understood [35]. Lucio-Garcia et al. [36] proposed the reactions between iron and H_2S as below:

The dissociation of hydrogen sulfide:

$$\mathrm{H_2S} \leftrightarrow \mathrm{H^+} + \mathrm{HS^-} \qquad (2\text{-}11)$$

$$\mathrm{HS^-} \leftrightarrow \mathrm{H^+} + \mathrm{S}^{2-} \qquad (2\text{-}12)$$

The cathodic reaction is the reduction of hydrogen sulfide:

$$\mathrm{H_2S} + 2\mathrm{e^-} \leftrightarrow \mathrm{H_2} + \mathrm{S^{2-}} \qquad (2\text{-}13)$$

The anodic reaction is still the oxidation of iron:

$$\mathrm{Fe} + 2\mathrm{e}^{-} \leftrightarrow \mathrm{Fe}^{2+} \qquad (2\text{-}14)$$

The next step is the formation of iron sulfide, which is of great significance in the H_2S corrosion process by governing the corrosion mechanism. Various iron-sulfur compounds with different crystal structures can be generated under the effect of some critical factors such as reaction times, temperature and pH [35].

These solid corrosion products consist of mackinawite (FeS), cubic ferrous sulfide (FeS), troilite (FeS), pyrrhotite (Fe_{1-x}), pyrite (FeS_2), smythite (Fe_9S_{11}), and greigite (Fe_3S_4) [36].

Different corrosion products play different roles in the corrosion process due to their diverse crystal structures and properties. Minor changes in temperature and H_2S concentrations can lead to transformations among these corrosion products, thus contributing to the prevention or facilitation of iron corrosion. Mackinawite is determined as the initial crystalline corrosion product [37], and it precipitates in relatively low temperatures and under H_2S partial pressure, displaying a tetragonal crystal structure. The layer of mackinawite is loose and porous, increasing conductivity but sometimes also increasing the restraint of anodic dissolution. With more exposure time, the metastable mackinawite film will undergo conversion into other compounds with better stability and anti-corrosion properties, such as troilite and cubic FeS. Pyrite will appear after much longer exposure times and exhibit the highest stability among varied forms of FeS. The stability and compactness of protective films formed by a multilayer of transformed sulfide can lead to an extensive reduction in the corrosion rate.

2.3 Corrosion mitigation methods

There are many effective methods and strategies to protect a pipeline and reduce the harmful effect of corrosion in the oil and gas industry. Four primary ways will be briefly introduced below. They are protective coatings, material selection, inhibitors and cathodic protection.

2.3.1 Protective coatings

Protective coatings are widely used to enhance the wear and corrosion resistance of the material. Protective coatings can be broadly divided into three categories: metallic coatings, organic coatings, and inorganic coatings. The protective functions can be performed by chemical inhibition, physical barrier protection and galvanic protection. An ideal multifunctional coating system should not only provide corrosion protection but also provide good adhesion and abrasion resistance.

In oil and gas production, a commonly used coating system is one made from fusion-bonded epoxy and a three-layer polyolefin on the surface of the material [38]. This type of coating is produced by heating the relevant power to a liquid form, applying the liquid on the surface of the material and, finally, solidifying the liquid. However, the coating is not suitable for the slotted liner of the SAGD system due to technical limitations.

An electroless Ni-P coating has been regarded as an effective approach to provide corrosion protection to the surface material in a wide range of environments [39]. Other advantages such as wear resistance, good adhesion, a relatively simple production process, and low costs also broaden the industrial applications of Ni-P coatings. The primary goal of this thesis is to develop a novel Ni-P-based coating with the incorporation of nanoparticles, further improving the performance of the Ni-P coating.

2.3.2 Other methods

Selecting the appropriate material is essential in corrosion protection. Every kind of metal and alloy has a different level of corrosion resistance, which is dependent not only on the properties of the material but is also highly influenced by the corrosion environment. The understanding of the corrosion environment is also important while selecting the material. When the material of construction is observed to be prone to corrosion damages, it is essential to alter this material and choose a suitable one to reduce the corrosion rate [40]. In industrial applications, various alloys such as stainless steel have been investigated and applied. Combining different elements and changing the chemical composition gives each kind of stainless steels particular mechanical property and anti-corrosion ability.

A corrosion inhibitor is a chemical that protects the material by retarding corrosion after being added to the corrosion environment. The inhibitor can work in different ways: (1) The inhibition can absorb on the surface of the material, restricting or eliminating the electrochemical process by blocking active sites on the surface. (2) The inhibition can facilitate the formation of a passive film, stifling the corrosion reactions on the surface. (3) The inhibition can react with other components in the environment, changing important conditions such as pH and ion concentrations.

The anti-corrosion properties of several inhibitors have been evaluated and studied in the presence of H_2S/CO_2 [3]. The results confirmed the high-level protection provided by these inhibitions, including fatty amides, imidazolines, and long-chain amines. The volatile corrosion inhibitor (VCL) also has also come to the attention of researchers because of its good performance [41]. Unlike conventional inhibitors, VCL can be injected into any part of the working system, and it will immediately form a physical bond on the surface and create a self-replenishing protective layer. It is essential to consider some important factors such as environmental issues, toxicity and costs before applying inhibitors.

The cathodic protection is another corrosion mitigation technique which changes the potential difference between the cathode and anode. Two major methods to apply cathodic protection include impressed current cathodic protection (ICCP) and the sacrificial anode. These two methods differ in how they minimize the potential gap [42].

ICCP is used to protect buried pipelines and shells of ships that come into contact with brine. An electric current is applied to the metal surface via a complete electrical circuit, and the current is impressed or forced by a power supply. To complete the circuit, the metal is connected to the negative terminal of the current source, and the positive terminal is connected to an auxiliary anode. The anode must be completely separated from the cathode. Once this situation occurs, a true electric circuit can be established with current flow from the anode to the cathode. Typical anodes are titanium coated with a mixed metal oxide or silicon iron, platinum, graphite and magnetite. The principle of the sacrificial anode cathodic protection is to use a more reactive metal in contact with the steel structure to make current flows from the anode to the cathode. When the current flows, all the corrosions occur on the anode, and the structure can be protected. This technique is frequently used for offshore oil production platforms.

2.4 Electroless Ni-P coating

2.4.1 Electroless plating

Ni-P coating can be synthesized using electroless plating and electroplating processes. In electroless plating, metallic ions are catalytically reduced when reducing agent is oxidized without external energy supply. In the electroplating process, the metal ions are reduced to initiate the deposition by using external electrical energy. One advantage of electroless plating is that the coatings that are obtained are of uniform thickness, and exhibit uniform physicochemical properties all over the plated object. Using electroless plating, this uniform coating can also be applied to components with complex shapes, which cannot be achieved by electroplating methods. Another benefit of the electroless coating is that it has better ductility. As a result, electroless plating has gained wide acceptance in the industry, and was selected as our primary method.

2.4.2 Substances in the plating bath

Electroless Ni-P plating is carried out in a plating bath containing a reducing agent, metal ions, complexants, stabilizer, buffers and wetting agents. There are also two significant parameters, pH and temperature, which should be in control during the plating process [43]. Table 2.1 exhibits these components and functions.

Table 2.1 Components of electroless nickel plating solutions and their functions.

Component	Function	Example
Metal Ions	Source of metal	Nickel Sulfate,
Reducing agents	Supply electrons to reduce the metal ions	Sodium hypophosphite
Complexants	Prevent excess free nickel ions and act as pH buffers	Dicarboxylic acids
Stabilizers	Prevent solution decomposition by shielding catalytically active deposition	Thioureas
Accelerators	Accelerate deposition	Fluorides
Buffers	Control pH	Sodium salt
Wetting agents	Increase wettability of plated surfaces	Surfactants
Temperature	Energy for deposition	85℃

2.4.3 Mechanism of deposition

The most commonly used reducing agent for electroless Ni-P coating is sodium hypophosphite. There are two widely accepted mechanisms for the deposition process in the plating bath containing hypophosphite [44].

The first one is an electrochemical mechanism, in which hypophosphite ions are catalytically oxidized, providing electrons at the catalytic surface and reducing hydrogen and nickel ions, as shown as follows.

Anodic reaction:

$$\mathrm{H_sPO_2^- + H_2O \rightarrow H_2PO_3^- + 2H^+ + 2e^-} \qquad (2\text{-}15)$$

Cathodic reaction:

$$\mathrm{Ni^{2+} + 2e^- \rightarrow Ni} \qquad (2\text{-}16)$$

$$\mathrm{2H^+ + 2e^- \rightarrow H_2} \qquad (2\text{-}17)$$

$$\mathrm{H_2PO_2^- + 2H^+ + e^- \rightarrow P + 2H_2O} \qquad (2\text{-}18)$$

The other is atomic hydrogen theory, in which hypophosphite is adsorbed on the surface and is catalytically dehydrogenated, releasing atomic hydrogen, as shown below.

$$\mathrm{H_2PO_2^- + H_2O \rightarrow HPO_3^{2-} + H^+ + 2H_{ads}} \qquad (2\text{-}19)$$

$$\mathrm{2H_{ads} + Ni^{2+} \rightarrow Ni + 2H^+} \qquad (2\text{-}20)$$

$$\mathrm{2H_{ads} \rightarrow H_2} \qquad (2\text{-}21)$$

$$\mathrm{H_2PO_2^- + H_2O \rightarrow H_2PO_3^- + H_2} \qquad (2\text{-}22)$$

$$\mathrm{H_2PO_2^- + H_{ads} \rightarrow H_2O + OH^- + P} \qquad (2\text{-}23)$$

2.4.4 Properties

The electroless Ni-P coatings have been used in different fields because of their remarkable properties such as high wear, corrosion resistance, and high hardness.

2.4.4.1 Structure

When the electroless Ni-P coating has a low or medium phosphorus content, the coating is both microcrystalline and amorphous. A high phosphorus content leads to a fully amorphous structure. However, heat treatment can significantly change the coating structure [45]. The structure of the coating can be crystallized from amorphous at a temperature above 220-260 ℃. When the temperature rises to 320°C, nickel phosphite begins appearing. The maximum crystallization of Ni-P coating can be achieved by heating the coating at 400°C for one hour. The final crystallized products of Ni-P coating after a heat treatment of 800°C are mixtures of the face-centered cubic nickel stable phase and Ni_3P [46].

2.4.4.2 Microhardness

Microhardness is related to a material's anti-wear properties. The microhardness of electroless Ni-P coating ranges from 500-650 $HV_{0.1}$, which is equivalent to the microhardness of varied hard alloys and is higher than that of electroplated coating [47]. The hardness can be further enhanced by heat treatment after crystallization of structure. The maximum value of coating hardness can be obtained by a 320°C-heat treatment for one hour or 260°C heat treatment for 10 hours.

2.4.4.3 Corrosion resistance

Corrosion protection is one of the most widespread applications of electroless Ni-P coating. These coatings can provide construction materials with decent corrosion resistance in different environments. Both the structure and the composition play important roles in Ni-P coating's anti-corrosion properties. Under the corrosion attack, the alloys with an amorphous structure are more stable than polycrystalline materials. The outstanding corrosion resistance of electroless Ni-P coating can also be ascribed to the phosphorus content. Previous studies [14,48] suggest that when the Ni-P coating is immersed in the corrosion environment, the nickel in the coating will dissolve into the solution. After that, the water in the solution can react with the phosphorus, forming adsorbed hypophosphite anions, preventing the nickel from dissolution.

2.5 Electroless Ni-P nanocomposite coating

Despite various benefits of electroless Ni-P coating, there are still some disadvantages. For example, hydrogen bubbles generated from the evolution reaction during the electroless deposition will create pinholes in the Ni-P coating's structure, which is harmful to the coating's protective ability. Thus, some strategies such as duplex coating and composite coating were developed to further improve the performance of Ni-P coating.

2.5.1 Introduction

Electroless Ni-P nanocomposite coating is produced by the co-deposition of the Ni-P matrix with nanoparticles, enhancing the properties of Ni-P coating, such as corrosion resistance and wear resistance. Nanoparticles possess a quantum size effect and many unique physicochemical properties. During the plating process, nanoparticles impinge and settle on the working surface, and are sequentially surrounded by the deposited Ni-P matrix [49]. No molecular bonding is formed between the incorporated particles and the Ni-P matrix.

In general, the Ni-P nanocomposite coatings can be divided into two categories depending on the properties of the embedded nanoparticles. The incorporation of some hard nanoparticles such as diamond ([50], TiO_2 [14], SiC [51], Al_2O_3 [52], SiO_2 [53]) can enhance the Ni-P coating's wear and corrosion resistance. On the other hand, lubricant particles such as graphite [54] and carbon nanoparticles [55] can reduce the Ni-P coating's friction coefficient.

Adding nanoparticles to the plating bath significantly increases the surface area loading, even resulting in the decomposition of the bath [56]. Suitable stabilizers have been applied to tackle this problem.

Some strategies have been employed to achieve a nanocomposite coating with good properties. The first important factor is choosing the suitable particle size. Large angular particles can result in rough surfaces. Nanoparticles can better modify the growth mechanism of the Ni-P matrix compared with micro-particles [57]. This is because when the particles are small, they can be firmly incorporated into the metallic matrix, leading to better integrity between nanoparticles and the matrix. Agitation should also be induced to keep the nanoparticles suspended in the plating bath, thereby regularly presenting these particles to the specimen. Another essential factor that influencing the plating process is the orientation of the specimen. The coating deposited on the surface of a vertically held specimen is more uniform than the coating growing on the horizontally held surface [58]. Surfactants such as sodium dodecyl sulfate (SDS) also important in the incorporation of nanoparticles because they make the nanoparticles wetter, thus making it easier for them to disperse. Other methods for incorporating nanoparticles are ultraviolet-visible (UV-vis) spectroscopy [59] and the ultrasonic probe [60].

2.5.2 Effect of nanoparticle concentration

The incorporation level of nanoparticles is highly influenced by the concentration of nanoparticles in the plating solution. For example, the incorporation of some nanoparticles [61] can be enhanced by increasing their concentrations in the plating bath up to a critical level, beyond which a continuously increasing concentration will cause saturation. The increase of flux of nanoparticles to impinge and deposit on the workpiece improves the incorporation level of nanoparticles. However, beyond the critical concentration, the agglomeration or grouping of nanoparticles occurs because of the decrease in the mean distance between each nanoparticle. The aggregation of nanoparticles will not only lead to their settling, it will retard the incorporation, which will negatively affect the coating’s properties.

2.5.3 Effect of nanoparticles on coating properties

2.5.3.1 Structure

The incorporation of most nanoparticles such as TiO_2 [62], SiO_2 [63], TiN [64], and Al_2O_3 [65] will not change the amorphous structure of the electroless Ni-P matrix because these nanoparticles are physically bonded with the matrix.

2.5.3.2 Microhardness

The hardness of composite coating can be improved by hard nanoparticles, and it is also influenced by the concentration of nanoparticles. An increased concentration of hard nanoparticles can increase microhardness. Sadreddini et al. [66] reported that SiO_2 nanoparticles were capable of significantly increasing the microhardness to 429 HV by the dispersion-hardening effect of nanoparticles, while the excessively high concentration of nanoparticles could lower this effect. Karthikeyan and Ramamoorthy [52] investigated the microhardness of electroless Ni-P-Al_2O_3 coating, confirming that nanoparticles could increase microhardness by retaining the mobility of the matrix dislocations and by retaining the dispersive amplification. The microhardness of coating can be further increased by heat treatment under 400°C, which results in the generation of the hard nickel phosphide phase (Ni_3P) in the Ni-P matrix.

2.5.3.3 Thickness

Nanoparticles' effect on the deposition rate is complex and can be shown by the thickness of the coating. Rahemi Ardakani et al. [67] argued that when the nanoparticles were concentrated in a reasonable range, they had sufficient opportunities to incorporate with the Ni-P matrix and worked as active points during the deposition process. With the nanoparticle concentration increasing within this reasonable range, the number of entrapped particles on the surface also increased, providing appropriate zones for coating growth and enhancing the coating's thickness. An excessive increase in the concentration of nanoparticles could cause the nanoparticles to aggregate, resulting in a higher viscosity of the plating bath, and reducing the coating thickness. However, Afroukhteh et al. [68] observed that a small concentration of TiC nanoparticles (0.01-0.1 g/L in the plating solution) reduced the deposition rate while a higher concentration (0.3 and 0.5 g/L) enhanced it. A low nanoparticle concentration enabled the cathode surface to be covered by TiC particles, hindering the diffusion of nickel ions from the solution to the working surface and retarding the precipitation of Ni-P coating [68]. When the nanoparticle concentration was higher, these nanoparticles were more likely to be trapped on the surface. The Ni-P coating deposition was promoted by the trapped nanoparticles on the interface, because they could act as active sites. Chen et al. [69] indicated that the incorporation of TiO_2 decreased the deposition rate and coating thickness.

In summary, there is no evidence that nanoparticle concentrations influence the precipitation rate and coating thickness. Therefore, it is important to investigate this effect because the thickness is closely related to the coating's mechanical and electrochemical properties.

2.5.3.4 Corrosion resistance

Structure defects exist in the Ni-P matrix. The corrosion process usually occurs from the surface to the substrate matrix through the pores or small defects within the coatings, and boundaries are the main path for aggressive ions during the corrosion process. Nanoparticles can act as nucleation points during the plating process, reducing the nodule sizes by blocking nodule boundaries, thus decreasing corrosion rate can be decreased [13]. However, the content of phosphorus in the coating decreases when the nanoparticle concentration is excessively high, reducing corrosion resistance of the coating.

Luo et al. [70] increased the corrosion resistance of coating by develop Ni-P-WC coating. Heakal et al. [71] employed nano-Al_2O_3 particles to enhance the corrosion resistance of Ni-P coating on an Mg alloy. The Al_2O_3 nanoparticles embedded in the Ni-P alloy can reduce the contacting area between coating surface and corrosive media, creating a potential physical barrier for corrosion in the aggressive sodium chloride environment.

The protective performance of electroless Ni-P/nano-SiC was also investigated by Soleimani et al. [72]. In a comparison, of electroless Ni-P and Ni-P-SiC coatings, the latter appeared to provide better corrosion protection. This can be ascribed to a reduction in the effective metallic area available for corrosion in the Ni-P-SiC coating [73]. SiC nanoparticles could easily fill defects and the penetration pathway of aggressive ions through the film to the interface.

Sharma et al. [74] regarded the decreased electrochemically active area as the reason for the improved corrosion resistance of the Ni-P-ZnO coating. Momenzadeh et al. [75] demonstrated that when the particles are co-deposited, the incorporation of particles could accelerate the passivation process of the nickel to improve the corrosion resistance of the composite coatings. Xu et al. [50] observed that the corrosion resistance of the Ni–P–nanodiamond (ND) coating was superior to that of the Ni–P coating because co-deposited nanoparticles prevent the corrosion pits from growing up. Improved resistance against pitting corrosion appears with the increased compactness of the coating.

In short, there are three main mechanisms behind the higher corrosion resistance of Ni-P nanocomposite coatings: decreasing the contact area between the coating surface and the corrosive media; blocking the penetration pathway of ions through the coating to the interface by filling defects; and increasing the compactness of coatings. However, few systematic investigations have examined the corrosion resistance of Ni-P nanocomposite coating in the corrosion environment containing H_2S and CO_2 with high temperatures and high pressure.

3. Methodology

3.1 Material preparations

3.1.1 Ni-P-WC coating

L80 carbon steel was used as the substrate to prepare the electroless Ni-P based coatings because L80 is widely used in the SAGD system. The specimen was cut into pieces that were 10 mm × 10 mm × 5 mm. WC nanoparticle powder (Inframat Advanced Materials) with 40-70 nm average particle size was used for composite coating.

Figure 3.1 shows the detailed steps taken during the electroless plating process. The surfaces of the sample pieces were ground by SiC paper from 200 to 1200 grit sequentially and degreased with acetone and distilled water between each grinding step. Before the electroless depositing, the surface was washed for 20 minutes in an alkaline solution which contained sodium carbonate/sodium hydroxide at 60 °C. Finally, the surface was pickled in 10 wt.% HCl solution for 60 seconds, enhancing the subsequent interaction between the activated surface and plating solution by facilizing the formation of surface active sites and removing the residential oxide. The main bath composition and electroless plating conditions are shown in Table 3.1. Figure 3.2 demonstrates schematic of the electroless plating process. The Ni-P coating was first deposited on the surface for 30 minutes, thus preventing the detrimental effect of agglomeration. After this, the

WC nanoparticles were added to the plating bath for continuous deposition for 90 minutes. Before being incorporated with Ni-P, the WC nanoparticles had been subjected to ultrasonic dispersion for 60 minutes. During the plating process, a magnetic motor stirrer was used to agitate the solution at a speed of 200 rpm.

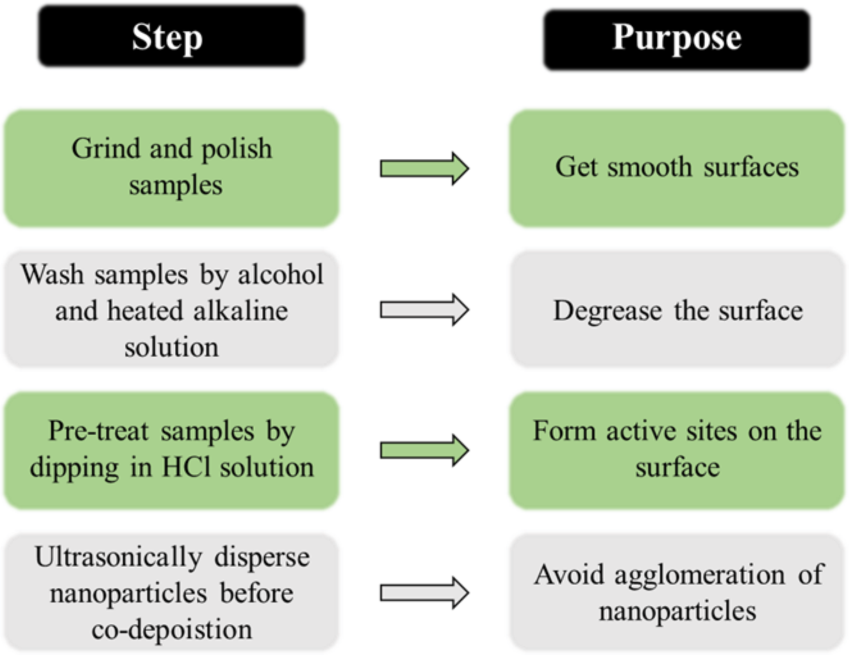

Step		Purpose
Grind and polish samples	⇨	Get smooth surfaces
Wash samples by alcohol and heated alkaline solution	⇨	Degrease the surface
Pre-treat samples by dipping in HCl solution	⇨	Form active sites on the surface
Ultrasonically disperse nanoparticles before co-depoistion	⇨	Avoid agglomeration of nanoparticles

Figure 3.1 Steps of the electroless plating process.

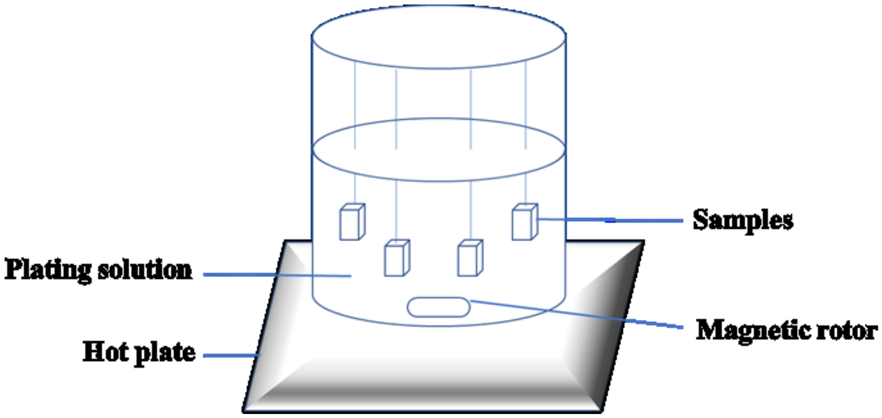

Figure 3.2 Schematic of the electroless plating process.

Table 3.1 Bath composition, functions of each chemical and electroless plating parameters for Ni-P and Ni-P-WC nanocomposite coatings.

Bath constituent	Function	Quality	Plating conditions
$NiSO_4 \cdot 6H_2O$	Nickel source	25 g L^{-1}	PH: 5.5-6.0
$NaH_2PO_2 \cdot H_2O$	Reducing agent	30 g L^{-1}	Agitation: 200 rpm
Lactic Acid	Complexing agent	20 mg L^{-1}	Temperature: 85 ℃
Citric Acid	Complexing agent	18-20 g L^{-1}	Time: ~120 min
Succinic Acid	Complexing agent	12-15 g L^{-1}	
Pb^+	Stabilizer	1 mg L^{-1}	
SDS	Surfactant	10 mg L^{-1}	
Saccharin	Grain growth inhibitor		
Nano-WC	Additive	0,1,3,5,7,10g L^{-1}	

3.1.2 Ni-P-Fe_3O_4 coating

From polishing to acid washing steps, the main pre-treatment process of preparing Ni-P-Fe_3O_4 coating was same with that of preparing Ni-P-WC coating. The Fe_3O_4 nanoparticle dispersed solution was provided by nFluids Inc. with 12 nm average particle size. In the dispersed solution, those spherical nanoparticles were capped with citric acid. The composition of the electroless plating bath and plating conditions are shown in Table 3.2. A different concentration of Fe_3O_4 nanoparticles was added to the plating solution. Before being incorporated with Ni-P, the Fe_3O_4 nanoparticles had been subjected to ultrasonic dispersion for 60 minutes. It is necessary to evenly distribute the nanoparticles within the coating. The final electroless process was performed for 120 minutes at 200 rpm.

Table 3.2 Bath composition and electroless plating parameters for Ni-P and Ni-P-Fe_3O_4 nanocomposite coatings.

Bath constituent	Concentration	Plating conditions
Nickel sulphate	25 g/L	pH: 5.5 - 6.0
Sodium hypophosphite	30 g/L	Temperature: 90 ± 1 ºC
Lactic acid	20 mL/L	Plating time: 120 min
Citric acid	18 g/L	Loading capacity: 1 dm^2/L
Succinic acid	14 g/L	Stirring speed: 200 rpm
Saccharin Sodium	0.08 g/L	
Sodium dodecyl sulfate	0.03 g/L	
Lead nitrate	1 mg/L	
Fe_3O_4 nanoparticles	0,0.4,0.8,1.5,3 g/L	

3.2 Electrochemical measurements

3.2.1 Three-electrode system

The three-electrode cell (Figure 3.3) is the most commonly used setup in electrochemistry. The three electrodes include the working electrode (WE), the counter electrode (CE) and the reference electrode (RE).

The working electrode is the electrode being studied and the one in which the concerned reaction takes place. In the corrosion experiments for this research, the working electrodes were either carbon steel, Ni-P coating, Ni-P-WC coating, or Ni-P-Fe_3O_4 coating.

The counter or auxiliary electrode is an electrode that completes the current circuit in the corrosion cell. Because the current flows between the CE and the WE, the CE acts as the electron's source/sink in most experiments, and the total surface of the CE should be larger than that of the

WE. This keeps the CE from being a limiting factor in investigated electrochemical reactions. Moreover, the CE is often fabricated from inert materials, and is usually not involved in the electrochemical reaction. The counter electrodes in the Ni-P-WC coating study were platinum, and in the Ni-P-Fe_3O_4 coating study they were graphite.

The reference electrode works as a reference point for the potential measurements in the corrosion cell. Therefore, the RE should have a stable potential for the electrochemical measurements. The stability of the RE is achieved by keeping the current flowing through the RE close to zero. This is accomplished by using the CE to close the current path. The stability is also achieved by using well-poised electrodes, where flowing current does not influence the potential. The well-poised electrodes have a redox system, where the concentrations of participants for the redox reaction are kept constant. The RE in this research was the silver/silver chloride electrode.

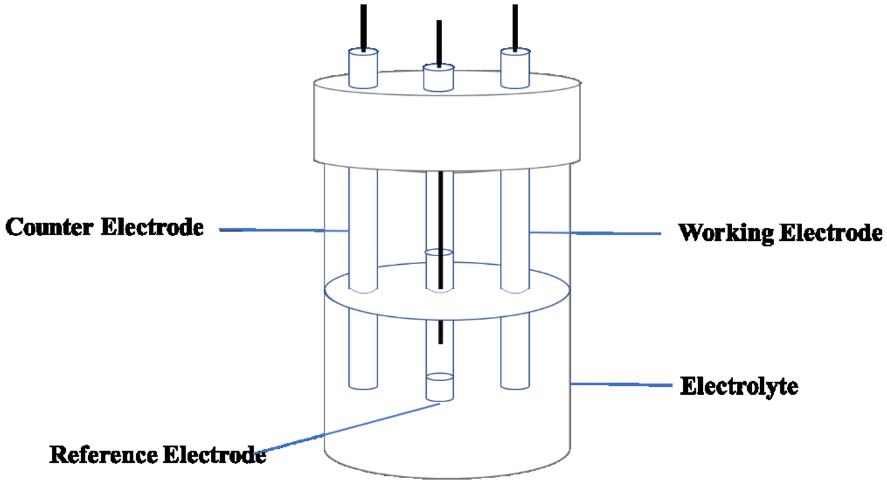

Figure 3.3 The schematic of a three-electrode system.

3.2.2 Potentiodynamic polarization

The potentiodynamic polarization measurements, based on electrochemical concepts, have been widely used to qualify electrochemical behaviors and determine corrosion rates [76]. This measurement method can provide important information about the corrosion process by monitoring the change in both the current and potential. The potentiodynamic polarization curve is a plot of the log current versus the potential.

Figure 3.4 illustrates a typical potentiodynamic polarization curve in the corrosion process and the use of a Tafel extrapolation method to obtain corrosion current and corrosion potential [77]. Obviously, the potentiodynamic polarization curve involves two major components: the anodic polarization curve and the cathodic polarization curve, corresponding to hydrogen evolution and metal dissolution, respectively. The log current versus the potential shows a linear relationship in both the anodic and cathodic polarization curves. This linear relationship called Tafel behavior results from the kinetics controlling the electrochemical reaction in the corrosion.

Extrapolating the liner portions of the anodic and cathodic sections will create a point of intersection where the corrosion potential (E_{corr}) and corrosion current (I_{corr}) can be obtained. A high corrosion current represents a high corrosion rate. However, there are sophisticated conditions that lead to complications which make it difficult/impossible to provide a linear section sufficient for accurate extrapolation. In this study, a more complicated fit was obtained by using analysis software from Gamry Instruments.

Carbon steel has poor corrosion resistance, and as a result, in the corrosive environment the current density will increase continuously as the potential increases. However, some alloys can form a passive protective layer on the metal surface during the corrosion process, as illustrated in Figure 3.5 [78]. In a wide potential range, the current increases only slightly because of the formation of the passive film, which highly enhances the material's anti-corrosion properties. In this study, the Ni-P nanocomposite coatings are expected to have a lower corrosion current, thereby indicating a decreased corrosion rate and better corrosion resistance.

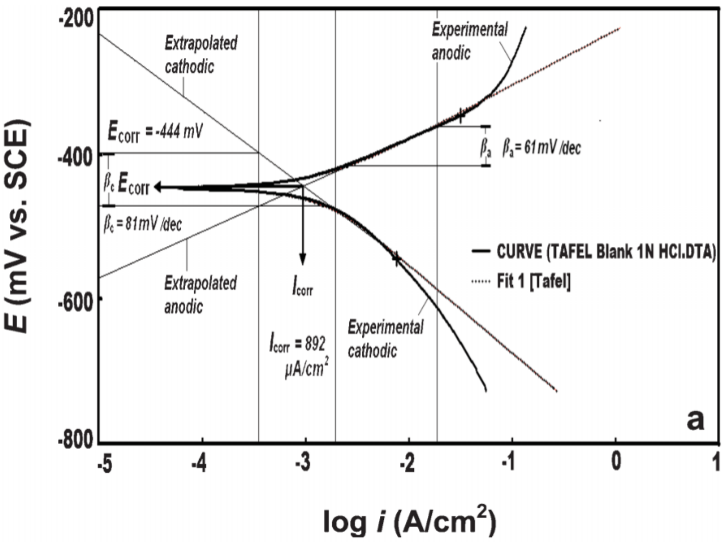

Figure 3.4 The Tafel extrapolation method for the potentiodynamic polarization curves to determine corrosion current and corrosion potential [77].

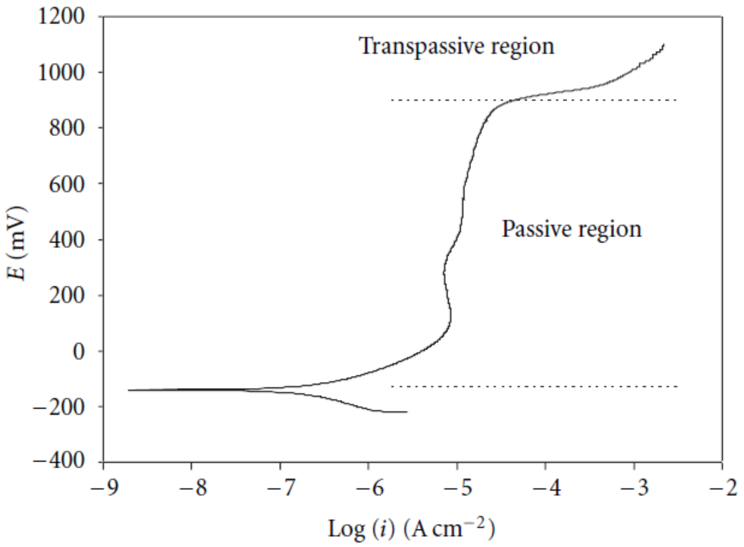

Figure 3.5 Potentiodynamic polarization curve for AISI 321 stainless steel in 0.5MH_2SO_4 [78].

3.2.3 Electrochemical Impedance Spectroscopy analysis

Electrochemical Impedance Spectroscopy (EIS) is a standard characterization method. Because of its extraordinary sensitivity, EIS has been widely used to evaluate corrosion behaviors of different materials [79]. Unlike potentiodynamic polarization, EIS is non-intrusive and will not damage the material's surface. In this method, various characteristic time constants of different electrochemical processes in the corrosion cell are shown under the influence of alternating current (AC) with different frequencies [80]. EIS measures the way in which a corrision cell with an AC responds to a broad range of frequencies. This reveals useful information about the underlying complex physical and chemical phenomenon.

Impedance (Z) can be calculated by Ohm's law as follows:

$$Z(\omega) = \frac{E(\omega)}{i(\omega)} \qquad (3\text{-}1)$$

E(ω) represents frequency-dependent potential, and i(ω) is frequency-dependent current. Z(ω) is a complicated quantity with a phase shift and magnitude, and it varies with changes in signal frequency. In the complex plane, the impedance can also be given by Equation 3-2:

$$Z_{total} = Z_{real} + Z_{imag} \qquad (3\text{-}2)$$

Z_{real} is the real part of impedance and Z_{imag} is the imaginary part of impedance. The absolute value of impedance can reflect a tested material's resistance to AC.

EIS data can be shown as a Nyquist plot (Figure 3.6) and a Bode plot (Figure 3.7) [80]. The Nyquist plot represents the real and imaginary parts of impedance, which are shown in the X axis and Y axis, respectively. The Bode plot illustrates the phase shift and absolute value of impedance in response to frequency. In this study, most EIS data was presented by Nyquist plots, because Nyquist plots could provide a quick overview and qualitative interpretations.

Equivalent circuit modeling consisting of well-known electrical components (e.g., capacitors (C), inductors (L), and resistors (R)) and distributed components (e.g., constant phase element (CPE) and Warburg impedance) can be used to further interpret the EIS analysis data and extract meaningful information about the corrosion cell. A typical equivalent circuit to explain the EIS data of carbon steel in the corrosive environment is shown in Figure 3.8. There are three electrical elements: the solution resistance (R_s), the constant phase element (CPE), and the charge-transfer resistance (R_{ct}). By comparing the EIS response of the equivalent circuit with the actual response of the corrosion cell, and obtaining a good fitting, the value of these elements can be determined.

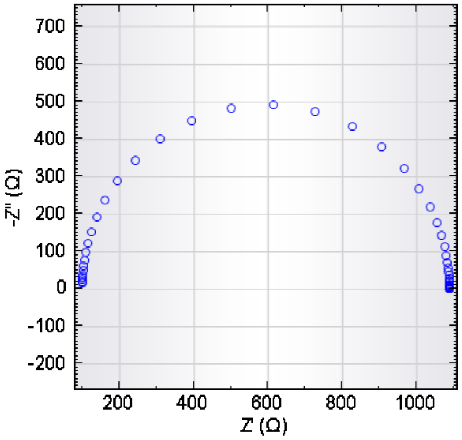

Figure 3.6 A typical Nyquist plot [80].

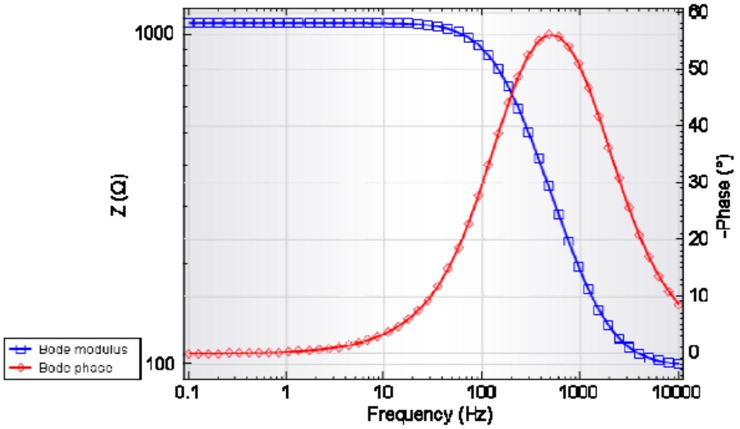

Figure 3.7 A typical Bode plot [80].

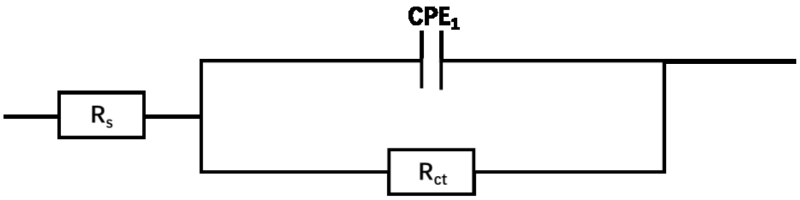

Figure 3.8 A typical Randles equivalent circuit for fitting the EIS data.

3.2.4 Electrochemical test conditions for Ni-P-WC coating

The electrochemical behaviors of the Ni-P coating and Ni-P-WC nanocomposite coatings were investigated in a National Association of Corrosion Engineers (NACE) standard TM0177-96 solution with H_2S and CO_2 (5 wt% NaCl+0.5 wt% acetic acid). N_2 gas was bubbled to the standard solution for three hours to remove the oxygen before introducing CO_2 and H_2S. After this, the CO_2 and H_2S were blown into the corrosion cell continuously for three hours to ensure that the solution was saturated with CO_2 and H_2S. During the testing, corrosive gases were also continually purged into the corrosion cell to supply the consumption of gases during the corrosion process. The corrosion cell used in this test is shown in Figure 3.9. The corrosion cell consisted of a three-electrode system, two inlet pipes, and an outlet pipe. The Gamry electrochemical workstation was used to conduct the electrochemical tests. A three-electrode system was constructed to perform the tests. The system consisted a platinum counter electrode, a saturated calomel electrode (SCE) reference electrode, and the sample as the working electrode. Prior to measurements, the samples were subjected to open circuit conditions for one hour until reaching a steady-state potential. The stable potential value obtained was considered the open-circuit potential (OCP). The EIS measurements started after the OCP was stable. The frequency was selected between 100 kHz and 10 mHz, with an applied AC amplitude of 10 mV. The impedance data were obtained by the equivalent electrical circuit using Zsimpwin software. The potentiodynamic polarization curves were measured with a scanning rate of 0.5 mV s^{-1} in the potential range of -0.3 V to 1 V with respect to the OCP. Each experiment was repeated more than three times under the same conditions to ensure reproducibility.

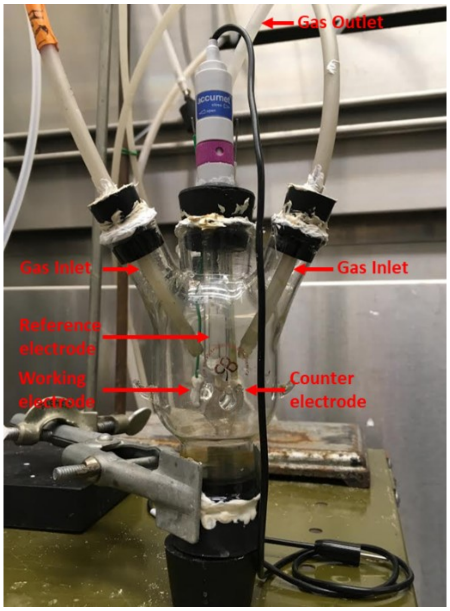

Figure 3.9 Electrochemical cell for corrosion tests.

The stability of coatings was also evaluated before and after being immersed for seven days. The coatings with different concentrations of WC nanoparticles had been immersed in a corrosion cell filled with 2500 ml 10^{-3} mol/L $Na_2S_2O_3$ + 0.5% acetic acid + 5 wt.% NaCl solution at room temperature for seven days. This solution can simulate the low concentration H_2S sour environment. This method was proposed for a study on the stress corrosion cracking of low alloy steels in the sour environment, and its reliability has been proved. The EIS measurements were conducted at an open-circuit potential with the frequency between 100 kHz and 10 mHz and an applied AC amplitude of 10 mV. The EIS tests were carried out after immersion for zero and seven days, respectively. The surface morphologies of coatings after immersion tests were also characterized by SEM.

3.2.5 Electrochemical test conditions for Ni-P-Fe_3O_4 coating

The coatings' electrochemical behavior was investigated by potentiodynamic polarization and EIS. The corrosion tests were conducted using a Gamry electrochemical workstation in a 3.5 wt.% NaCl solution. The set-up consisted of a conventional three-electrode cell with a carbon rod as the counter electrode and a saturated calomel electrode (SCE) as the reference electrode. Prior to measurements, the samples were subjected to open circuit conditions for one hour until they reached a steady-state potential. The EIS was measured at OCP, and the frequency selected was between 100 kHz and 10 mHz, with an applied AC amplitude of 10 mV. The impedance data were analyzed using an equivalent electrical circuit and Zsimpwin software. The potentiodynamic polarization curves were measured with a scanning rate of 0.5 mV s^{-1}, starting from −0.5 vs. OCP to +0.5 V vs. OCP potential. Each experiment was repeated more than three times under the same conditions to ensure reproducibility.

3.3 Immersion tests

The stability of the Ni-P-Fe_3O_4 coatings was evaluated using immersion tests at room temperature under normal pressure and autoclave tests at high temperature under high pressure. The coating chosen for the examination of coating stability was the one that had delivered the best performance in previous electrochemical tests. In the immersion tests, the specimen was mounted in epoxy (with an exposed area of one cm^2) and immersed in the 3.5 wt.% NaCl solution. The sample surfaces were cleaned before and after the test using acetone and distilled water. Morphologies of the coating surface were detected before and after immersion.

The capsule test was designed to tentatively evaluate the stability of the Ni-P coating and Ni-P-Fe_3O_4 coating, and it was conducted at 150°C in the 3.5 wt.% NaCl solution saturated with CO_2 gas for 240 hours. As shown in Figure 3.10, samples were sealed on a Teflon holder and placed in a capsule, which was heated by the furnace with the pressure kept at 0.48MPa. The samples were cleaned with deionized water and acetone, and weighed before being installed in the capsule. After 10 days, they were rinsed with deionized water and acetone and observed using OSM.

The high-temperature, high-pressure corrosion test was conducted at 120 °C in the 3.5 wt.% NaCl solution saturated with CO_2 gas for 192 hours. As shown in Figure 3.11, the samples were hung on a holder in the autoclave, which was heated with a total pressure kept at four MPa (0.8 MPa CO_2 and 3.2 MPa N_2). The samples were cleaned with deionized water and acetone before being installed in the autoclave. After eight days, they were rinsed with deionized water and acetone, and their surfaces were examined using SEM. Before and after the corrosion test, the weight of the specimen was accurately measured using an electronic balance with an accuracy of 0.1 mg.

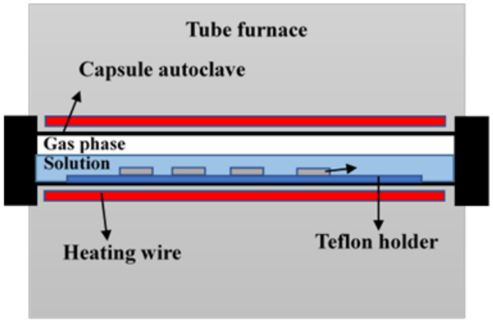

Figure 3.10 Schematic diagram of the apparatus for the capsule test.

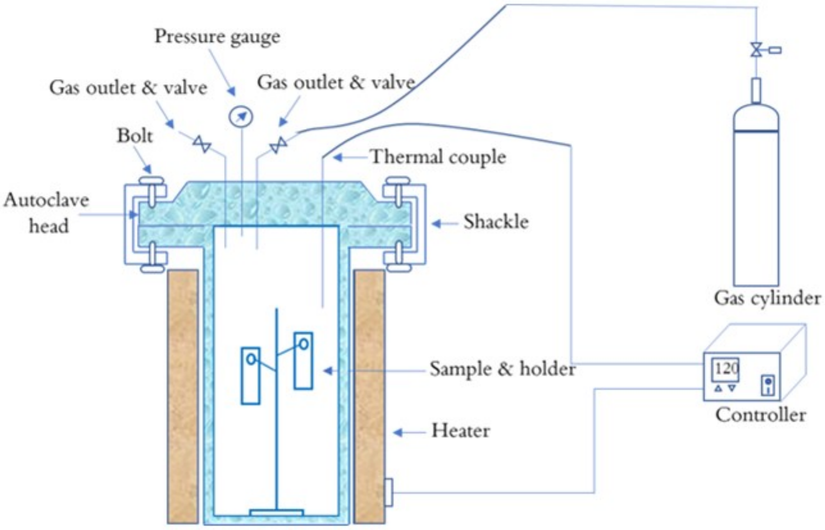

Figure 3.11 Schematic diagram of the apparatus for the corrosion test under high temperature and high pressure.

3.4 Material characterization

The surface morphologies and cross-sections of Ni-P, Ni-P-WC and Ni-P-Fe_3O_4 coatings were evaluated using OSM and SEM. The composition of coatings was investigated by EDS. The crystalline structure of coatings was characterized by XRD with Cu Kα radiation.

3.4.1 Morphology

An optical stereoscopic microscope (OSM) and scanning electron microscope (SEM) were used to record the highly magnified images of surface morphologies on the specimen. The light source of OSM is visible light, and OSM employs a series of lenses to magnify images of small features. A camera will capture and collect the images. OSM can also provide surface topography information via a three-dimensional visualization of a specimen, which is accomplished by using separate objective lenses and eyepieces.

However, the max magnification of OSM is only 1000X. When a more detailed image of the surface morphology is expected, SEM is a more useful technique. Unlike OSM, a SEM is a type of electron microscope. It generates images of a specimen by scanning the surface with an electron beam.

In SEM, the electrons are generated from the gun and accelerated to a range of energy [81]. The beam is focused by electron lenses, producing a sharp image. The beam passes through the final lens into the specimen chamber, where it interacts with the specimen at various depths on the surface, producing signals that contain important topography information. When the emitted electrons interact with atoms, different types of signals such as secondary electrons (SE) and back-scattered electrons (BSE) are generated on the surface. In general, a SE emerges from a very shallow depth beneath the specimen surface, while a BSE is involved with elastic scattering and is generated from a deeper location. The SE images were used in this thesis due to their better resolution.

3.4.2 Energy-Dispersive X-ray Spectroscopy

Energy-Dispersive X-ray Spectroscopy (EDS or EDX) is an analytical technique used to characterize the chemical composition and element distribution of a specimen, and is usually coupled with SEM. Under the effect of a high energy beam, the electrons of the inner shell of an atom will be excited and escape from the shell, simultaneously forming an electron hole. The electrons from outer and high energy shells will drop to the inner shell and fill the hole. The energy difference between the outer and inner shells will be released in the form of an X-ray. By measuring the energy of the characteristic X-rays, the presence of elements and their relative concentrations can be determined.

3.4.3 X-ray diffraction

X-ray diffraction (XRD) is a non-destructive characterization technique that can be used to investigate the crystallographic structure and chemical composition of a specimen. The working principle of XRD is to record the X-ray diffraction caused by impacting the crystalline atoms. The angles and intensities of these beams can reveal significant structural information, such as defects and dislocations. The two major modes of XRD are powder diffraction and thin film diffraction. The incident angle of the X-ray beam in powder diffraction is in a larger range (0° to 90°), while the angle of the incident beam in thin film diffraction is fixed within a smaller range (< 5°).

3.4.4 Microhardness tests

The microhardness of the Ni-P-WC coatings was analyzed by a Vickers microhardness tester. The employed loading weight was 100 grams and the load time was 10 seconds. The results were calculated from the average of five measurements.

The indenter is the essential component of the tester. It is made from material that is highly resistant to self-deformation. A diamond in the shape of a square-based pyramid is commonly used. An example of the indentation formed during the testing process is shown in Figure 3.12. The hardness can be calculated automatically by the instrument itself through an equation as follows:

$$HV = \frac{1.8544\,F}{d^2} \qquad (3\text{-}3)$$

F represents the weight load in kilogram force and *d* is the average, in millimeters, of two diagonals caused by the indenter.

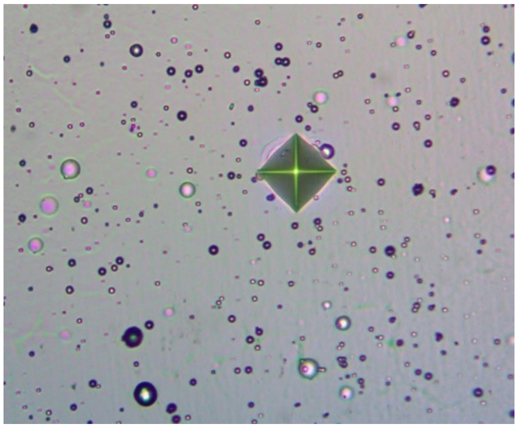

Figure 3.12 The indentation generated by the Vickers microhardness indenter on the Ni-P coating surface.

4. Influence of WC nanoparticles on hardness and corrosion resistance of electroless Ni-P coating

4.1 Introduction

Carbon steel can be used as engineering material in the petroleum industry. However, it is likely to suffer from degradation as a result of corrosion, wear, friction, and erosion, which results in significant financial losses. Therefore, different surface treatment methods are applied to improve carbon steel’s corrosion resistance and extend its service life. Effective surface modification methods include anodization protection, electroplating, electroless plating, and PVD. Of these, electroless plating and electroplating are the two most common processes. Unlike complex electroplating, electroless plating is relatively simple and can be used to create a uniform deposition on irregularly shaped components.

The electroless deposition of Ni-P is an autocatalytic reduction on metals and alloys. Ni-P acts as a barrier to isolate the substrate from the outside corrosive environments and shows high corrosion and wear resistance as well as uniform coating thickness. The coating's structure and property are mainly dependent on the concentration of deposited P. The structure of Ni-P-related coatings can be transformed from amorphous to nano-crystalline after heat treatment, improving the microhardness and wear resistance. Thus, Ni-P coating is considered an effective method to modify the physical and chemical properties of substrates.

There are also several methods to further improve the properties of the coating to meet special demands. For example, introducing metallic elements such as Cu, W, Mo, and Zn into the Ni-P coating can significantly impact the microstructures and properties of coatings. Developing duplex coating can also enhance mechanical and anti-corrosion properties.

Co-depositing nanoparticles (e.g., SiC, Al_2O_3, SiO_2 and Si_3N_4) [82] is a good method to further improve the performance, such as wear resistance, of Ni-P coatings. The WC is a type of hard particle with superior physical and chemical properties. WC can be employed in many fields. Incorporating WC nanoparticles has been reported to improve erosion resistance, thermal conductivity, and mechanical properties. However, few systematic studies have investigated the effect of adding WC to facilitate corrosion resistance. The goal of my research is to study how the concentration of WC nanoparticles influences the morphology, hardness, and corrosion properties of Ni-P- based coatings in order to better understand the role that WC nanoparticles play in the Ni-P matrix.

4.2 Results and discussion

4.2.1 Surface characterization

Figure 4.1 shows the surface morphologies of the electroless Ni-P coating and Ni-P/nano-WC coatings with different concentrations of WC nanoparticles, which indicates that the morphologies were strongly influenced by the amount of WC nanoparticles. As presented in Figure

4.1(a) and (b), the surface of the Ni-P coating was relatively smooth, and typical spherical growth features of the Ni-P coating could be observed.

However, the surface of the coating tended to be rougher after the WC nanoparticles were added. From Figure 4.1(b) to (h), with increasing nanoparticle concentration, the density of spherical nodular structures also increased.

When the concentration of the WC nanoparticles was 1 g/L, the surface of the Ni-P coating was not sufficiently covered by overlapping packages caused by WC particles. When the nano-WC concentration reached 5 g/L, the distribution of particles was uniform, and the surface was fully covered by the Ni-P/nano-WC composite coating. Nevertheless, with the further increase of the nanoparticle concentration to 10 g/L, the agglomeration of the packages was obvious, and the surface was much more porous. The agglomeration was not effectively prevented even in the presence of magnetic agitation and surfactant because the WC concentration in the bath solution exceeded a critical level. Beyond this level, the WC nanoparticles will be aggregated due to the decreasing mean distance between each other, causing the nanoparticles to settle. Moreover, as nanoparticles can act as nucleation centers of the package during when the electroless Ni-P coating is forming, the spherical nodule on the coating surface will also aggregate.

Fig. 4.2 shows the uneven surface of the Ni-P/nano-WC (10 g/L) composite coating as seen through the 3D function of the OSM. The agglomeration of nanoparticles resulted in the formation of peaks, suggesting the harmful effect of aggregation on surface uniformity.

The elemental composition of the electroless Ni–P coating and Ni-P/nano-WC (5 g/L) composite coating is shown in Figure 4.3. As shown in Figure 4.3 (b), the peak for W was detected, confirming that the WC was incorporated in the Ni-P matrix.

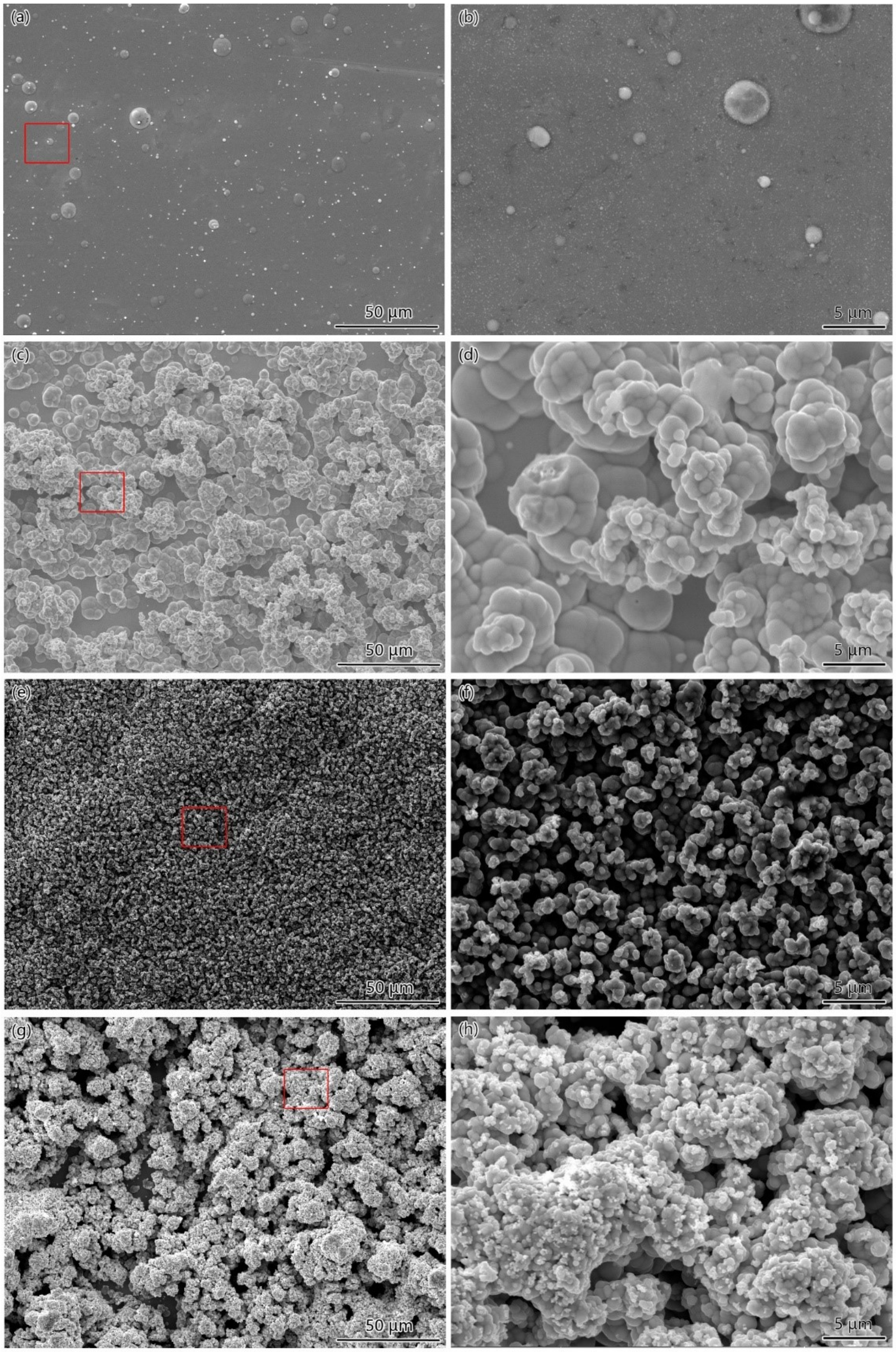

Figure 4.1 SEM images of electroless (a) Ni-P coating, (b) higher magnified image of Ni-P coating, (c) Ni-P-WC (1 g/L) composite coating, (d) higher magnified image of Ni-P-WC (1

g/L) composite coating, (e) Ni-P-WC (5 g/L) composite coating, (f) higher magnified image of Ni-P-WC (5 g/L) composite coating, (g) Ni-P-WC (10 g/L) composite coating, (h) higher magnified image of Ni-P-WC (10 g/L) composite coating.

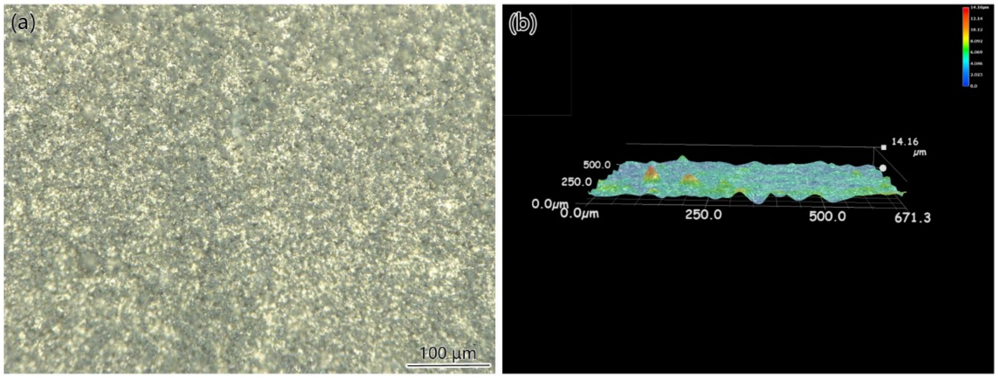

Figure 4.2 (a) OSM morphologies of the Ni-P-WC (10 g/L) composite coating, and (b) 3D-OSM morphologies of Ni-P-WC (10 g/L) composite coating.

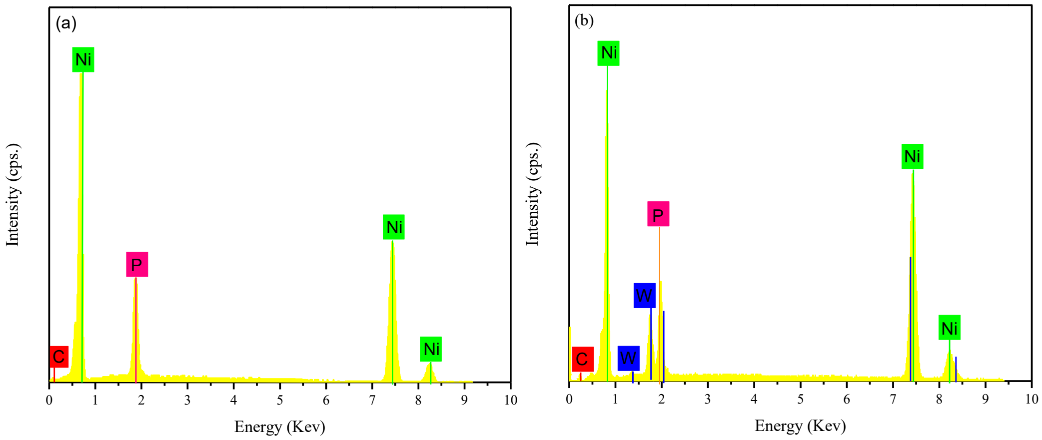

Figure 4.3 EDS analysis of the (a) Ni-P coating and the (b) Ni-P-WC (5 g/L) composite coating.

4.2.2 Electrochemical behaviors

4.2.2.1 Potentiodynamic polarization curves

To evaluate the electrochemical behaviors of the Ni-P coating and the Ni-P-WC nanocomposite coatings, potentiodynamic polarization curves were measured in the NACE standard TM0177-96 solution with H_2S and CO_2, as shown in Figure 4.4. The corrosion current density was obtained using Tafel's extrapolation method. The fitting values of corrosion current density and the corrosion potential of coatings are listed in Table 4.1.

As shown in Figure 4.4, the corrosion potential of Ni-P-WC nanocomposite coatings showed different degrees of positive shift, compared with that of the Ni-P coating, suggesting that the corrosion tendency was reduced when the WC nanoparticles were incorporated. Correspondingly, the corrosion current densities decreased noticeably, suggesting an increase in corrosion resistance. No passivation process was seen in any of the polarization lines. The Ni-P coating revealed the highest corrosion current density of ~4.04×10^{-5} A·cm$^{\mathbf{-2}}$. When the concentration of nanoparticles increased to 5 g/L, the corrosion current density decreased noticeably to 4.93×10^{-6} A·cm$^{\mathbf{-2}}$, suggestion the highest inhibition efficiency. Nevertheless, adding more WC nanoparticles slightly increased the corrosion current density.

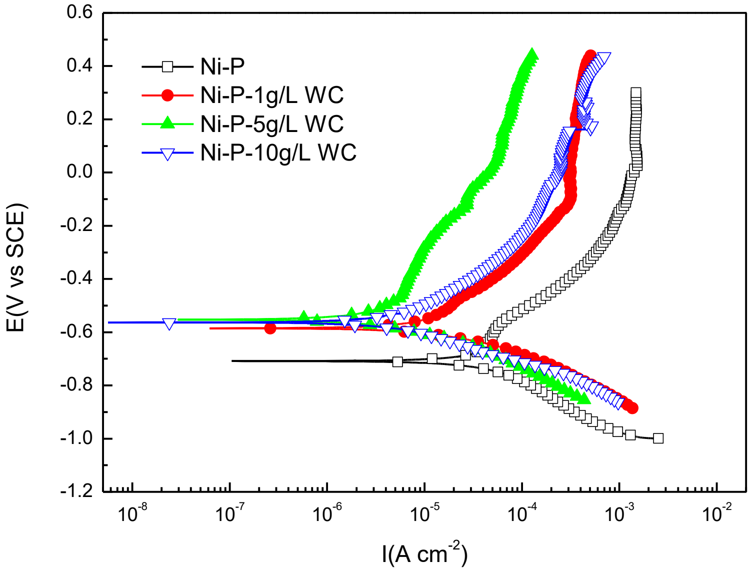

Figure 4.4 Potentiodynamic polarization curves of coatings in the NACE standard TM0177-96 solution with H_2S and CO_2.

Table 4.1 Corrosion current density and corrosion potential of Ni-P and Ni-P-WC nanocomposite coatings in the NACE standard TM0177-96 solution with H_2S and CO_2.

Samples	***E*corr** (V vs. SCE)	***I*corr** ($A \cdot cm^{-2}$)
Ni-P	-0.709	4.04×10^{-5}
Ni-P-1g/L WC	-0.585	1.17×10^{-5}
Ni-P-5g/L WC	-0.553	4.93×10^{-6}
Ni-P-10g/L WC	-0.563	5.72×10^{-6}

It is well known that Ni-P can protect a substrate from corrosion media by acting as a physical barrier, which can block corrosive media. Furthermore, Ni in the coating can be preferentially dissolved in corrosive media, enrichening phosphorus on the surface. A $H_2PO_2^-$ layer is formed from the reaction between enriched phosphorus and H_2O, blocking the access of water to the coating and inhibiting nickel hydration.

However, there are still defects such as small pores and grain boundaries within the Ni-P coating. These are harmful to the coating's anti-corrosion properties. Incorporating WC nanoparticles could fill up the tiny pores in the Ni-P coating, forming a more compact coating, cutting the corrosion path, and minimizing the contact of aggressive ions. Moreover, the nanoparticles work as nucleation points during the plating process, which cuts off the nodule boundaries and decreases the nodule sizes. The nodule boundaries are main corrosion paths. This suggests that the structure with co-deposited WC can remarkably improve the Ni-P coating's corrosion resistance.

However, excessive nanoparticles will lead to the aggregation and settlement of joint particles. The agglomeration of nanoparticles will not only destroy the uniformity of the coating surface but also increase the contact area between the surface and corrosive media, as seen in Figure 4.2. This can explain why the corrosion resistance showed a decrease when the nanoparticle concentration reached 10 g/L.

4.2.2.2 EIS analysis

Figure 4.5 shows the EIS spectra of different coatings in the NACE standard TM0177-96 solution with H_2S and CO_2. As shown in Figure 4.5, the Nyquist plots for Ni-P coatings with different concentrations of WC nanoparticles displayed a similar shape of a single semicircle with different scales in the investigated frequency range, indicating that a similar electrochemical process occurred on the coating surfaces. The diameter of the capacitance loop is associated with the polarization resistance of the coating. The diameters of all Ni-P-WC nanocomposite coatings were larger than that of Ni-P coating, which demonstrated better corrosion resistance in the corrosion environment. When the nanoparticle concentration rose from 1 g/L to 5 g/L, the diameters of the capacitive arcs also increased. This occurred because more nanoparticles were deposited with Ni-P coating with the increasing WC concentration. However, a greater increase in nanoparticle concentration caused a slight decrease in the diameters of the capacitive arcs.

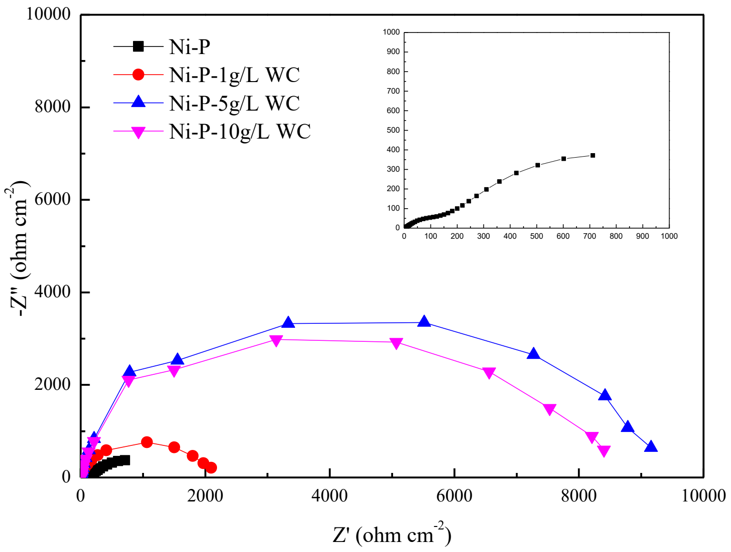

Figure 4.5 Nyquist plots for the Ni-P coating and Ni-P-WC nanocomposite coatings in the NACE standard TM0177-96 solution with H_2S and CO_2.

Different models have been proposed to explain the EIS spectra for Ni-P-related coatings [83,84]. The corresponding equivalent circuit shown in Figure 4.6 was used to fit EIS results and determine relevant electrochemical parameters. R_s corresponds to the resistance of the solution between the reference electrode and the working electrode. $R_{coating}$ is the resistance of the coating and R_{ct} represents the charge transfer resistance. CPE_1 corresponds to the capacitance of the double layer formed on the surface, and CPE_2 is the coating capacitance.

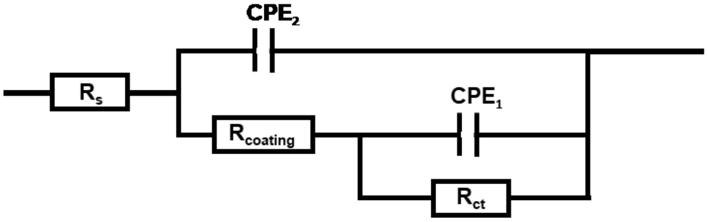

Figure 4.6 The equivalent circuit for the Ni-P coating and Ni-P-WC nanocomposite coatings in the NACE standard TM0177-96 solution with H_2S and CO_2.

The best fitting values of electrochemical parameters are listed in Table 4.2, which shows that the values of CPE_1 and CPE_2 for all the coatings varied consistently. The CPE_1 and CPE_2 of the Ni-P-WC coatings reduced significantly compared with that of the Ni-P coating. The decreased CPE_1 demonstrated a lower porosity and a more compact coating. The lowest value was generated by the Ni-P-WC coating formed in the plating solution containing 5 g/L WC nanoparticles.

R_p ($R_{coating}$+R_{ct}) can represent the polarization resistance of the coating during the corrosion process, which was inversely related to the corrosion rate. The highest $R_{coating}$ and R_{ct} also came from the Ni-P-5g/L WC coating, suggesting that this coating had the highest corrosion resistance and the lowest corrosion rate. The EIS results were consistent with the results from the potentiodynamic polarization curves.

Table 4.2 The electrochemical parameters fitted from EIS data by using the equivalent circuit.

Coatings	R_s ($\Omega\cdot cm^2$)	CPE_1 ($\Omega^{-1}\ cm^{-2}\ s^{-n}$)	R_{coat} ($\Omega\cdot cm^2$)	CPE_2 ($\Omega^{-1}\ cm^{-2}\ s^{-n}$)	R_{ct} ($\Omega\cdot cm^2$)
Ni-P	5.343	3.74×10^{-4}	167.8	3.23×10^{-3}	1556
Ni-P-1g/LWC	5.417	2.18×10^{-5}	1554	1.60×10^{-3}	643.2
Ni-P-5g/L WC	5.415	1.63×10^{-5}	5534	1.04×10^{-4}	3558
Ni-P-10g/L WC	5.248	2.55×10^{-5}	5401	1.50×10^{-4}	3205

4.2.3 Stability in the stimulated solution

4.2.3.1 EIS analysis

Figure 4.7 shows EIS plots obtained for the Ni-P and Ni-P-WC nanocomposite coatings with different WC contents before and after the immersion test. As showed in Figure 4.7(a), before the immersion the Nyquist curves for all coatings consisted of a semicircle and appeared similar shapes but different sizes. This implies that same fundamental corrosion process occurred on the surfaces of all these coatings, but that the effective area in each case differed. The size of the semicircle was proportional to the anti-corrosion property of the coating [85]. Apparently, when the nanoparticle concentration increased from 0 to 5 g/L, the size of the semicircle also increased noticeably. However, when the concentration exceeded 5 g/L, the higher number of nanoparticles caused a decrease in the size of the semicircle. This trend was also observed in Nyquist plots for all coatings after being immersed for seven days, as depicted in Figure 4.7(b). It is noted that sizes of the semicircles reduced slightly after seven-day immersion.

The equivalent circuit used to explain the Nyquist plots and determine the relevant parameters in the stimulated solution was the same as the equivalent circuit in Figure 4.6. The values of R_p ($R_{coating}$+ R_{ct}) are listed in Table 4.3.

As mentioned before, the R_p was the sum of the coating resistance (R_{coat}) and charge transfer resistance (R_{ct}), and a higher R_p could represent the better anti-corrosion ability of the coating. It is clear that adding the WC nanoparticle led to the significant increase of R_p, indicating that the corrosion resistance improved. However, the anti-corrosion ability of all of the coatings deteriorated under the destructive ions in the simulated solution. Although R_p for some Ni-P-WC coatings changed more significantly than R_p for the Ni-P coating, the R_p values of most Ni-P-WC coatings were still much higher than that of the Ni-P coating, further confirming that the Ni-P-WC coatings were more stable in the long-term corrosion process. The Ni-P-WC nanocomposite coating with 5 g/L still exhibited the best stability, consistent with the previous results.

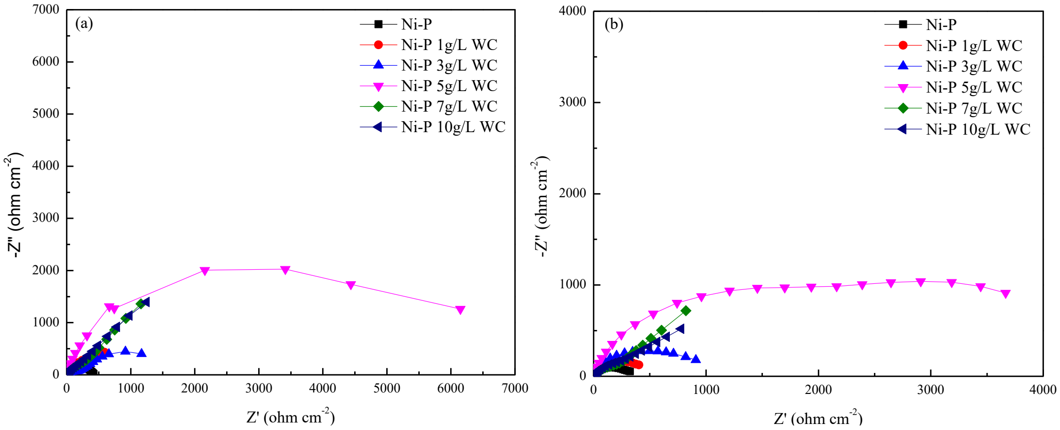

Figure 4.7 Nyquist plots for Ni-P and Ni-P-WC coatings in the simulated solution (a)before and (b)after seven days immersion.

Table 4.3 The values of R_p fitting from EIS data by employing the equivalent circuit model.

Samples	**R_p ($\Omega \cdot cm^2$) before immersion**	**$R_{p'}$ ($\Omega \cdot cm^2$) after immersion**
Ni-P	423	369
Ni-P-1g/L WC	1765	743
Ni-P-3g/L WC	2356	1058
Ni-P-5g/L WC	7603	6017
Ni-P-7g/L WC	6633	2980
Ni-P-10g/L WC	5595	2553

4.3.3.2 Surface morphologies

Morphologies of coating surfaces are shown in Figure 4.8. The long-term corrosion had an obvious impact on the coating surfaces. As shown in Figure 4.8 (a), Ni-P coating was subjected to severe localized corrosion. A large number of corrosion pits were induced, and they even contributed to the rupture of the Ni-P coating. This indicates that the Ni-P coating was susceptible to localized corrosion. Conversely, the deposition of corrosion products was observed around the nodule structures on the surface of the Ni-P-WC coating, and no obvious localized corrosion was found, suggesting that the Ni-P-WC coating had better corrosion resistance. This protective layer formed by the corrosion product could make the coating more stable, preventing the Ni from dissolving further.

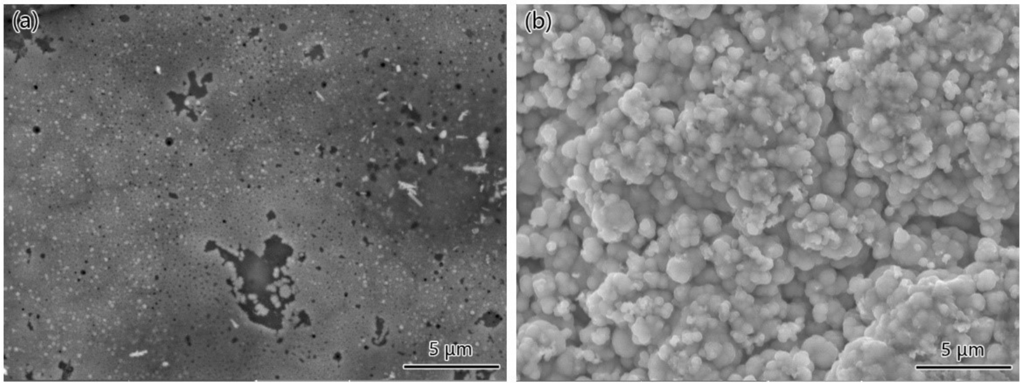

Figure 4.8 Surface morphologies of (a) the Ni-P coating, and (b) the Ni-P-WC (5 g/L) coating after seven-days immersion in the simulated solution.

4.2.4 Microhardness of the coating

Hardness is an important mechanical parameter that contributes to how effectively a material resists scratches and dents. According to the literature, heat treatment can play a significant role in the microhardness of Ni-P-related coatings [86,87]. Hence, Ni-P and Ni-P-WC coatings were heated at 400 °C, 500 °C and 600 °C for one hour in a nitrogen atmosphere. The values of microhardness are shown in Figure 4.9.

Figure 4.9 shows that the Ni-P-WC nanocomposite coatings generally had higher microhardness than the Ni-P coating, suggesting that the incorporation of the WC nanoparticles enhanced the microhardness. The co-deposited WC particles can be the second phase in the Ni-P matrix, and work as a barrier to obstruct the plastic deformation and retard the dislocation motions. The enhanced microhardness of the Ni-P-WC coating could also be due to the dispersion hardening effect resulting from the high hardness of the WC nanoparticles. In the concentration range of 0 g/L to 5 g/L, the microhardness of the coating increased as the concentration increased. However, the microhardness of the coatings decreased with nanoparticle concentrations larger than 5 g/L, due to the harmful effect of agglomerated nanoparticles.

After being annealed at high temperatures, all the coatings exhibited higher microhardness. The precipitation hardening occurred during heat treatment when the amorphous Ni-P transformed into crystallites of Ni_3P [88]. However, some literature reported that excessively high temperatures might cause aggregating and coarsening of the grain size, decreasing the coating's microhardness.

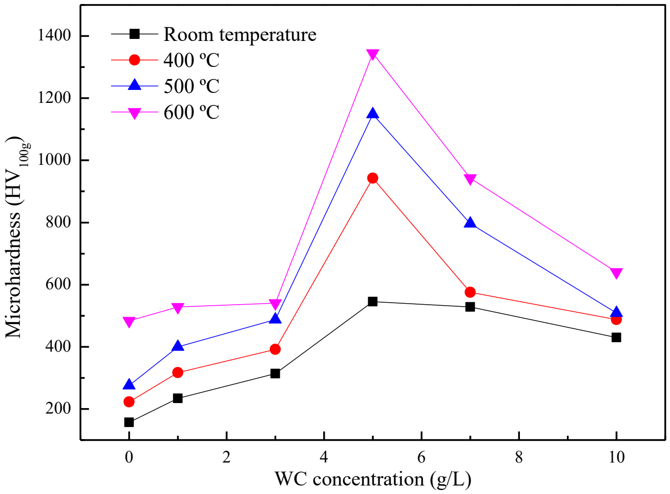

Figure 4.9 The microhardness of as-prepared Ni-P and Ni-P-WC coatings and those annealed at 400 °C, 500 °C, 600 °C.

4.3 Conclusions

The concentration of WC nanoparticles had an impact on the morphologies, microhardness, and electrochemical properties of the coatings.

(1) When the concentration was higher than a critical level, aggregation was induced and

created a porous surface.

(2) In the H_2S and CO_2 environments, the Ni-P-WC coatings were more resistant to corrosion than the Ni-P coating.

(3) Adding WC increased the hardness of the coating. Heat treatment also significantly improved the microhardness.

(4) The optimized concentration of WC in the plating bath for microhardness and electrochemical performance was 5 g/L. A higher nanoparticle concentration was harmful to the coating properties.

5. Development and characterization of electroless Ni-P-Fe_3O_4 nanocomposite coating

5.1 Introduction

Carbon steel be used to produce slotted liners in the Steam Assisted Gravity Drainage (SAGD) system. However, carbon steel is susceptible to severe corrosion in a complex high- temperature environment containing CO_2, H_2S, and brine. A wide range of surface modification methods have been developed to improve carbon steel's corrosion resistance and extend the material's service time, thereby reducing production costs.

Using electroless plating to obtain nickel-phosphorous (Ni-P) coating is the most predominantly used method in many engineering applications due to its inherently unique properties such as high corrosion resistance, wear resistance, uniform thickness, and high hardness [48,89,90]. Another significant benefit of electroless plating is that it can be suitable even for components with complex shapes [91]. According phosphorous content in the coating, these Ni-P coatings can be classified into three types: low, medium, and high [14, 92]. Low phosphorus coatings possess high hardness whereas coatings with high phosphorus content exhibit good corrosion resistance [93].

Nevertheless, there are many pinhole defects in electroless Ni-P coating due to the hydrogen bubbles that evolve during the deposition process. These bubbles have a harmful effect on the corrosion resistance of coatings [72]. An effective method to solve this problem and further improve the physical and chemical properties of the coating is to incorporate nanoparticles in the matrix [73]. Nanoparticles possess many well-known and unique properties because of their quantum size effect. Nanoparticles co-deposited with Ni-P coating can be divided into two categories. Hard nanoparticles such as WC, SiC, Al_2O_3, B_4C, SiO_2, and TiO_2 have been used to increase hardness, wear resistance, and corrosion resistance [69, 72, 94, 95]. Soft nanoparticles such as MoS_2 and WS_2 can also be added to the plating bath to produce lubricating composite coatings [96, 97]. Selecting appropriate nanoparticles can lead to composite coatings with highly specific characteristics and desirable service parameters.

The Fe_3O_4 is a type of hard particle with favorable properties such as high corrosion resistance, nontoxicity, low cost, environmental friendliness, and natural abundance. Hence, Fe_3O_4 nanoparticles are widely used for therapeutics [98, 109], battery material [100], and as catalysts [101]. However, limited investigations have been conducted to examine the design of embedding Fe_3O_4 particles in high phosphorous electroless coating. This study focuses on the fabrication, properties, and performance of Ni-P-Fe_3O_4 coatings on an L80 carbon steel substrate. The properties of the Ni-P coating and Ni-P-Fe_3O_4 coating with different nanoparticle concentrations in the bath were analyzed by SEM using EDS, XRD, potentiodynamic polarization, and EIS. The influence of the nanoparticle concentration on the morphology, thickness, and corrosion resistance of the coating was discussed in this report, and an optimized concentration was obtained. The anti-corrosion properties of the Ni-P coating and the optimized Ni-P-Fe_3O_4 coating were further compared by a long-term corrosion test, and the corrosion mechanism was investigated.

5.2 Results and discussion

5.2.1 Surface morphology and composition of the coatings

The morphologies of Ni-P coating and Ni-P-Fe_3O_4 coatings with different amounts of nanoparticles are depicted in Figure 5.1. All of the coatings showed a crack-free surface. Their surface morphologies were closely related to the concentration of Fe_3O_4 in the plating solution. Figure 5.1 (a) shows the pores distributed on the smooth surface with some spherical nodules, especially at the boundaries. When the nanoparticle concentration was low (0.4 g/L), there was no significant change in the morphology. Most nanoparticles can be observed at the boundary of nodules, where they block some coating defects. Fe_3O_4 nanoparticles had been embedded in the Ni-P matrix via co-deposition. Figure 5.1 (c) shows that when the concentration reached 0.8 g/L, the surface was almost fully covered by the coating, and few defects could be observed. The surfaces became rougher, and nano-Fe_3O_4 particles were distributed randomly. The grain size decreased to a smaller value as Fe_3O_4 could act as new growth zones. When the concentration of Fe_3O_4 was less than 0.8 g/L, the surfaces of the coatings were relatively smooth. However, large nodular structures were found when more Fe_3O_4 was added. Increasing the concentration of Fe_3O_4 nanoparticles (1.5 g/L) and incorporating them changed the surface morphology significantly. Some spherical globules overlapped each other. The magnified image in Figure 5.2 (d) showed that the grain size of coating was also much larger. The contact area between the coating surface and corrosion media increased, which created a problem because localized corrosion is more likely to occur on a non-uniform surface. In addition, there were cracks around the edge of nodular parts, which is problematic because the cracks expose the material to more corrosion. When the Fe_3O_4 concentration exceeded a certain level (0.8 g/L), the agglomeration of nanoparticles played an important role [102], even with ultrasonic dispersion and magnetic agitation, and coating grew around the agglomeration sites and made the surface an uneven.

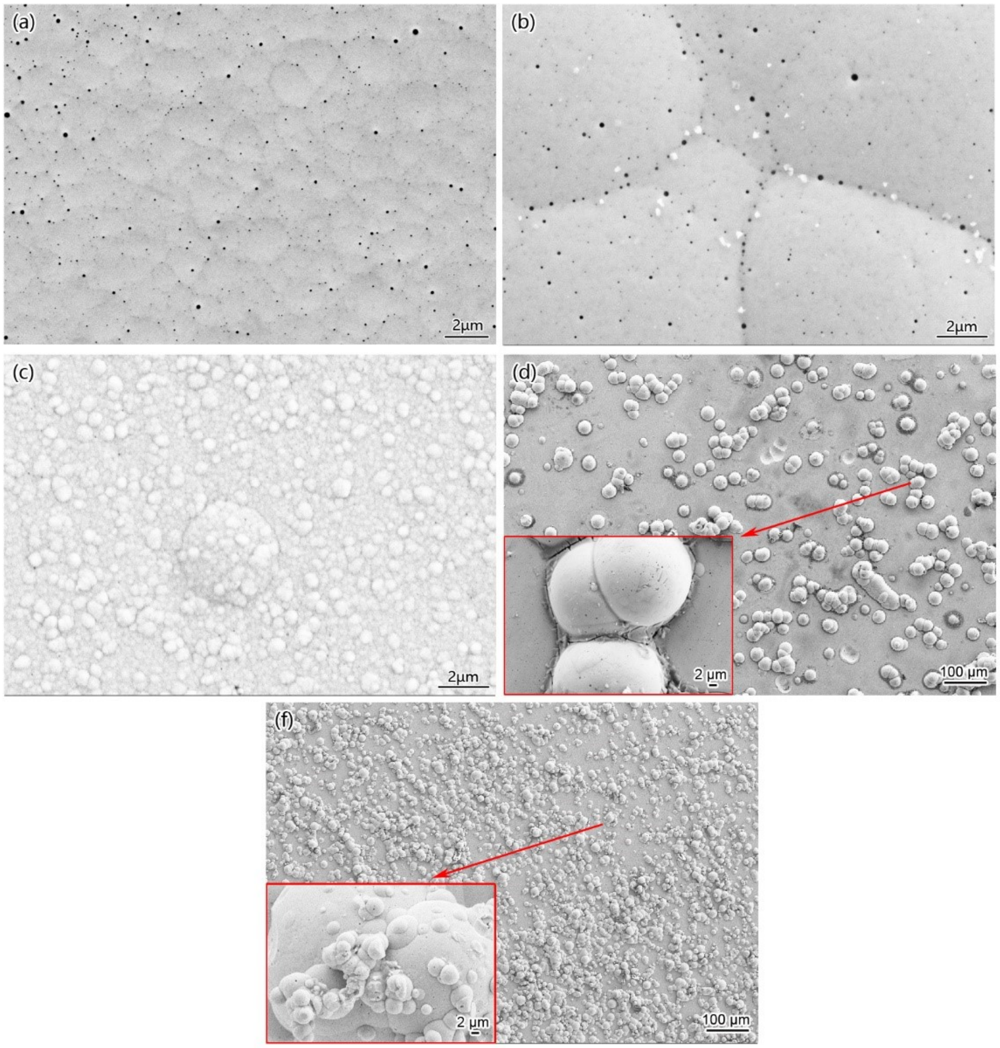

Figure 5.1 Morphologies of coatings investigated by SEM (a) Ni-P, (b) Ni-P-Fe_3O_4(0.4 g/L), (c) Ni-P-Fe_3O_4(0.8 g/L), (d) Ni-P-Fe_3O_4(1.5 g/L), (d) Ni-P-Fe_3O_4(3.0 g/L).

To further confirm the existence of Fe_3O_4 in the nano-composite coating, an EDS analysis of coating surfaces was carried out. Fig. 5.2 shows the spectra. The iron peak was detected with a nickel peak and phosphorous peak, confirming the presence of Fe_3O_4 nanoparticles in the Ni-P matrix. Table 5.1 shows the composition of nickel and phosphorous in the coatings. The addition of Fe_3O_4 slightly reduced the phosphorous content, but the nanocomposite coating was still highly phosphorus.

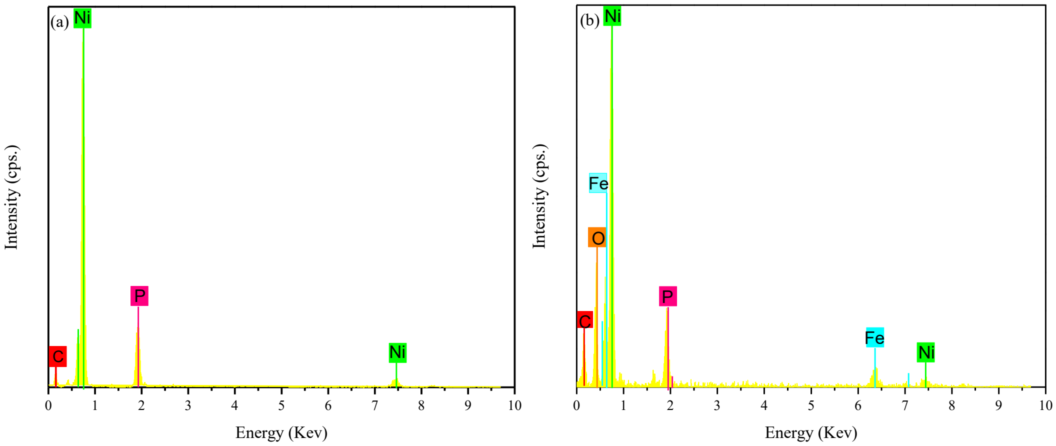

Figure 5.2 EDS spectra of (a) Ni-P coating, and (b) Ni-P-Fe_3O_4(0.8 g/L) coating.

Table 5.1 Composition of Ni-P coating and Ni-P Fe_3O_4 coating determined by EDS.

Type of coating	Nickel (wt%)	Phosphorous (wt%)
Ni-P	84.19	15.71
Ni-P-Fe_3O_4 (0.8g/L)	87.19	12.8

Figure 5.3 shows the XRD results of the Ni-P-Fe_3O_4 nanocomposite coating with the Fe_3O_4

concentration of 0.8 g/L. There was a broad diffraction peak at the 40~50° angle due to the amorphous status of the Ni-P coating [103]. No crystalline Fe_3O_4 characteristic peak could be recognized because of the superposition of amorphous Ni-P peaks and the extremely low amount of Fe_3O_4 within the coating [60,104]. However, SEM images (Figure 5.3) and EDS results (Figure 5.4) showed the existence of Fe_3O_4 in the nanocomposite coating.

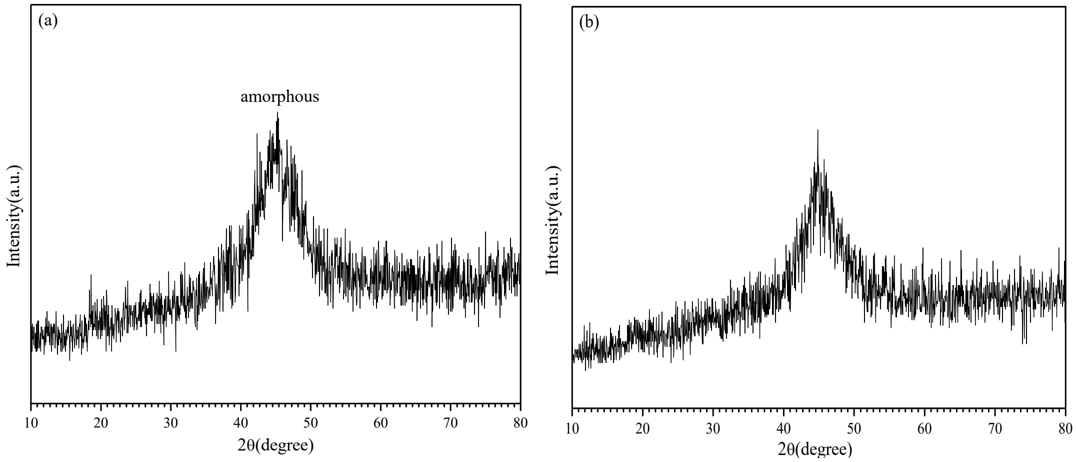

Figure 5.3 XRD spectra of (a) Ni-P, (b) Ni-P-Fe_3O_4(0.8 g/L) coating.

5.2.2 Thickness of the coatings

Figure 5.4 shows that the surfaces of Ni-P, Ni-P-Fe_3O_4 (0.4 g/L), and Ni-P-Fe_3O_4 (3.0 g/L) coatings were smooth and uniform. However, with a higher concentration of nanoparticles, uneven surfaces occurred, which was consistent with results of previous surface morphology studies. No obvious Fe_3O_4 nanoparticles can be observed in Figure 5.4, likely because they are too small to see.

Table 5.2 shows the values of thickness for different coatings. The concentration of nanoparticles significantly influenced the deposition rate of the coating. The deposition rate for the Ni-P coating was measured at 7.6 μm/h. When the concentration of Fe_3O_4 was lower than 0.8 g/L, the addition of a nanoparticle to the plating solution increased the deposition rate. The highest co-deposition rate, 9.5 μm /h, was obtained from the specimen co-deposited with 0.8 g/L.

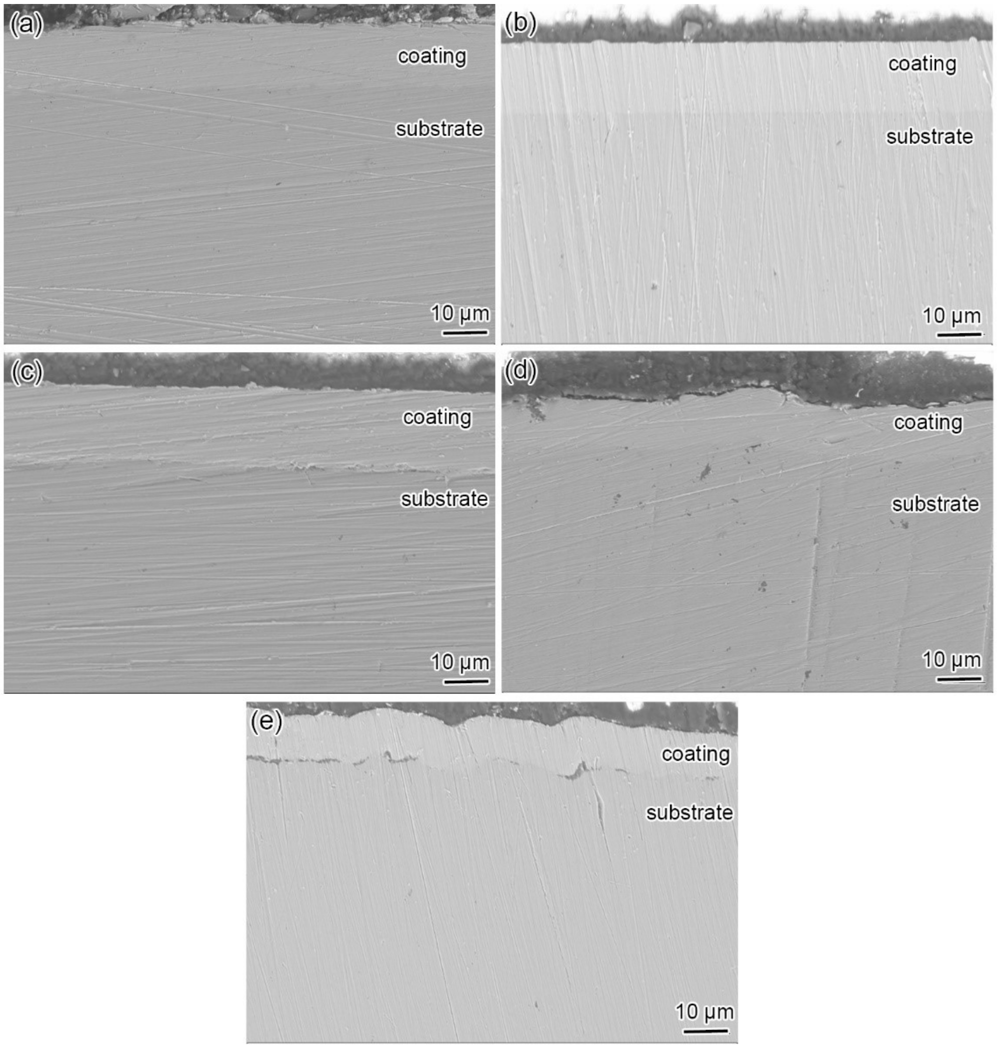

Figure 5.4 Cross-section of Ni-P-Fe_3O_4 composite coatings plated from baths with different concentrations of nanoparticles: (a) 0 g/L, (b) 0.4 g/L, (c) 0.8 g/L, (d) 1.5 g/L (e) 3.0 g/L.

Fig. 5.5 shows the electroless plating process on the substrate surface as a way of explaining the difference in thickness and surface morphologies between the Ni-P coating and Ni-P-Fe_3O_4 nanocomposite coatings. As shown in Figure 5.5 (a), the electroless deposition of the Ni-P coating is accomplished by nickel and hypophosphite ions. Figure 5.5 (b) shows that when the nanoparticle concentration is not excessively high, particles have sufficient opportunity to be embedded in the coating and these entrapped particles can work as active zones, increasing the deposition rate and coating thickness. Nevertheless, the deposition rate drops dramatically with the further addition of Fe_3O_4 and decreases steadily as the concentration of Fe_3O_4 in the system increases, as depicted in Figure 5.5 (c). One explanation is that when the nanoparticle concentration exceeds a level (0.8 g/L), nanoparticles are more likely to cover the cathode surface, which suppresses the diffusion of Ni^{2+} ions from the solution to the substrate, decreasing the co-deposition rate. A higher nanoparticle concentration can also lead to agglomeration and a higher viscosity of the solution, lowering the deposition rate. [40, 89]. Furthermore, the aggregation of nanoparticles could destroy the uniformity and smoothness of the surface.

Table 5.2 Difference in thickness of coatings with varied nanoparticle concentration.

Fe_3O_4 concentration (g/L)	**Thickness (μm)**
0	15.2
0.4	17.6
0.8	18.9
1.5	11.8
3	10.9

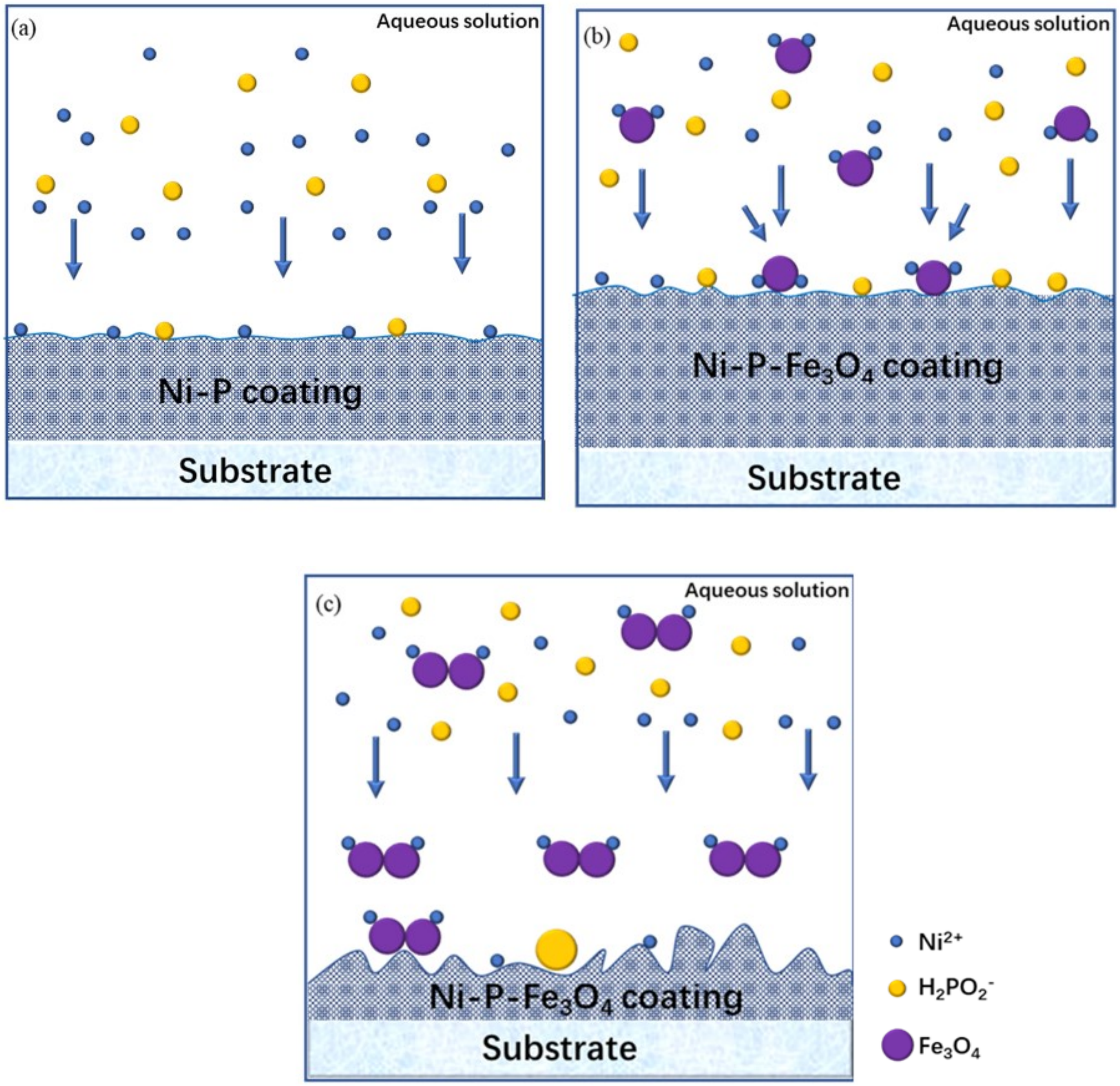

Figure 5.5 The coating formation process in plating solutions with different Fe_3O_4 nanoparticle concentrations (a) 0 g/L, (b) 0.8 g/L, (c) 3 g/L.

5.2.3 Electrochemical corrosion performance

5.2.3.1 Potentiodynamic polarization curves

The effect of the Fe_3O_4 concentration on the coating's corrosion behavior was evaluated using potentiodynamic polarization curves. Figure 5.6 shows potentiodynamic polarization curves of Ni-P-Fe_3O_4 nanocomposite coatings containing different amounts of nano-Fe_3O_4 particles. Table 5.3 shows the results calculated using the Tafel extrapolation method.

As shown in Figure 5.6, the corrosion potential was shifted toward a positive direction in the presence of nano-Fe_3O_4 particles. Also, according to the polarization curve, the Ni-P-Fe_3O_4 composite coatings had lower corrosion current density than the Ni-P coating. This suggests that they possess better corrosion protection in salty environments.

As seen in Table 5.3, adding Fe_3O_4 nanoparticles increases the corrosion potential, promoting a more positive potential value and decreasing the corrosion current density. Moreover, the Ni-P coating revealed the highest corrosion current density of ~3.24 $\mu A\cdot cm^{-2}$. This indicates that all the nanocomposite coatings showed higher corrosion resistance than the Ni-P coating. When the Fe_3O_4 nanoparticle concentration was below 0.8 g/L, the I_{corr} gradually decreased as the concentration in the plating solution increased. Furthermore, the I_{corr} decreased noticeably to its minimum value (0.693 $\mu A\ cm^{-2}$) when the Fe_3O_4 content increased to 0.8 g/L. Nevertheless, with the increase of the Fe_3O_4 concentration to 1.5 g/L, the I_{corr} slightly increased to 0.922 $\mu A\cdot cm^{-2}$. When the concentration of Fe_3O_4 reached 3.0 g/L, the I_{corr} further increased to 1.1 $\mu A\cdot cm^{-2}$, showing that the coating's corrosion resistance had decreased. Among all nanocomposite coatings, the most efficient inhibition was obtained for the coating that formed in the plating bath containing 0.8 g/L nano-Fe_3O_4 particles.

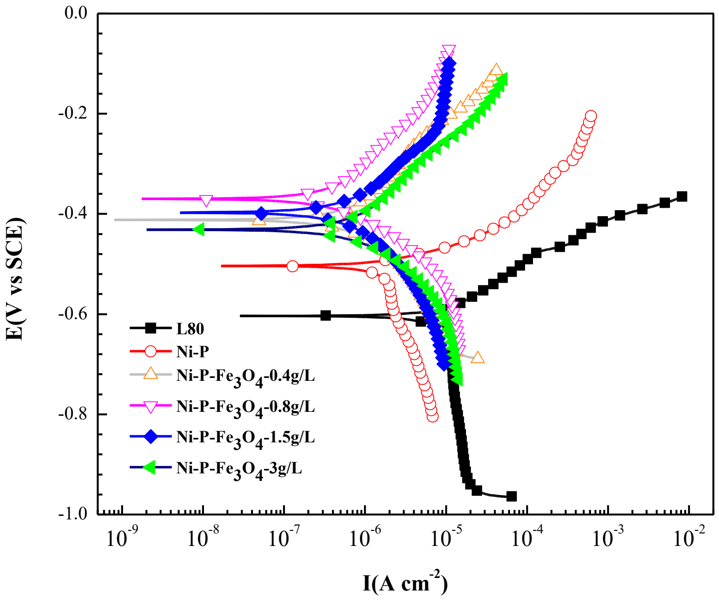

Figure 5.6 Potentiodynamic polarization curves of coatings in the 3.5 wt.% NaCl solution.

Table 5.3 Corrosion characteristics of Ni-P coating and Ni-P-Fe_3O_4 coatings in 3.5 wt.% NaCl.

Samples	E_{corr} (V vs SCE)	I_{corr} ($\times10^{-6}$ A·cm^{-2})
L80	-0.604	11.3
Ni-P	-0.532	3.24
Ni-P-Fe_3O_4-0.4g/L	-0.417	1.26
Ni-P-Fe_3O_4-0.8g/L	-0.368	0.693
Ni-P-Fe_3O_4-1.5g/L	-0.394	0.922
Ni-P-Fe_3O_4-3.0g/L	-0.442	1.1

5.2.3.2 EIS analysis

Figure 5.7 presents the Nyquist plots of the substrate and coated specimens obtained at open circuit potential in 3.5 wt.% NaCl solutions. The Nyquist plots for all specimens showed similar shapes of a single semi-ellipse in the frequency range from 10 kHz to 0.01 Hz, suggesting that the same electrochemical process occurs on the surfaces. But the radius of the curves showed that each coating had a different corrosion resistance. With the introduction of Fe_3O_4 nanoparticles to the Ni-P coating, the radii of the capacitive arcs of the Ni-P-Fe_3O_4 coatings were larger than those of the Ni-P coating, indicating that the Ni-P-Fe_3O_4 coating exhibited better corrosion resistance. When the nanoparticle concentration increased up to 0.8 g/L, the radius of the curve reached the highest value.

The equivalent circuits depicted in Figure 5.8 are used to simulate and describe corrosion property parameters of the substrate and coatings [74]. The equivalent circuit denoted solution resistance (R_s), coating resistance ($R_{coating}$), charge transfer resistance (R_{ct}), admittance associated with the double layer capacitance (CPE_1), and coating capacity (CPE_2). The best fitting values of R_{ct} and R_1 based on the equivalent electric circuit are listed in Table 5.4.

As shown in Table 5.4, the R_p (R_{ct}+$R_{coating}$) of the Ni-P coating was significantly higher than that of the substrate. With the nano-Fe_3O_4 particles incorporated in the Ni-P coating, the R_p values of the Ni-P-Fe_3O_4 coatings were several times greater than those of the N-P coating. For coatings with a concentration of Fe_3O_4 nanoparticles under 0.8 g/L, the value of R_p increased when the concentration of nanoparticles increased. When the concentration of nanoparticles was 0.8 g/L, R_p reached the maximum value (76290 $\Omega\cdot cm^2$) among all coatings, which meant it had the best corrosion resistance. Nevertheless, there was a gradual decrease in the R_p value as the nanoparticle concentration increased further. The corrosion trend of the coatings presented in the electrochemical impedance data was in good agreement with the results obtained from the potentiodynamic polarization curves.

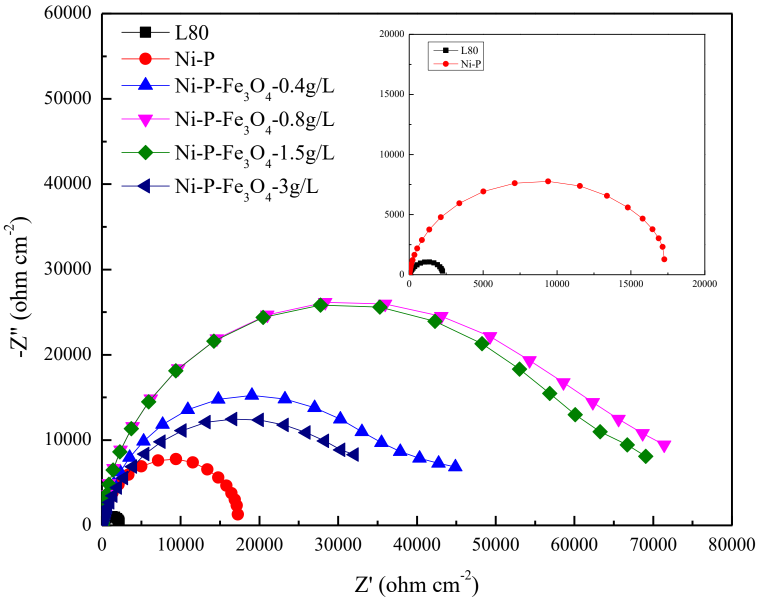

Figure 5.7 Variation in the Nyquist curves as a function of the concentration of Fe_3O_4 in 3.5 wt% NaCl solution.

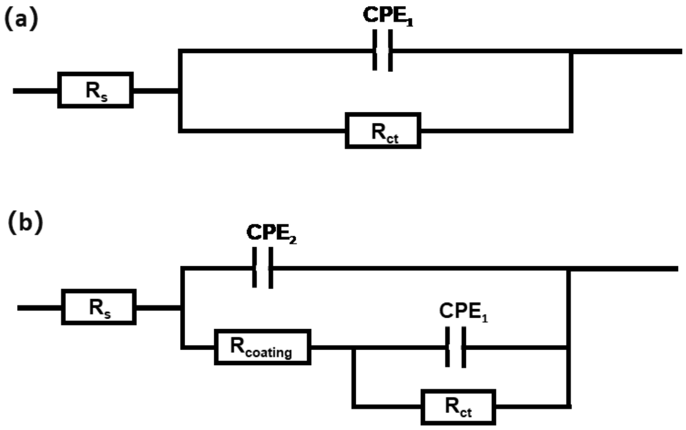

Figure 5.8 Equivalent circuits for (a) substrate, (b) Ni-P and Ni-P-Fe_3O_4 coatings in 3.5 wt.% NaCl solution.

Table 5.4 Equivalent circuit parameters for impedance spectra

Material	R_p($\Omega\cdot cm^2$)	$R_{coating}$ ($\Omega\cdot cm^2$)	R_{ct} ($\Omega\cdot cm^2$)
L80	2610	-	2610
Ni-P	18299	10880	7419
Ni-P-Fe_3O_4 (0.4g/L)	44812	372	44440
Ni-P-Fe_3O_4 (0.8g/L)	76290	39110	37180
Ni-P-Fe_3O_4 (1.5g/L)	69740	40500	29240
Ni-P-Fe_3O_4 (3.0g/L)	36387	517	35870

5.2.4 Stability of Ni-P-Fe_3O_4 coating

5.2.4.1 Immersion test at room temperature under normal pressure

From the above results, it can be concluded that adding Fe_3O_4 will further improve the Ni-P coating's corrosion resistance and that the Ni-P-Fe_3O_4(0.8 g/L) coating performs best in anti-corrosion property. Further experiments are needed to prove that the Ni-P-Fe_3O_4 coating is stable enough to provide long-term corrosion protection.

As shown in Figure 5.9, SEM detected the morphologies of coatings after immersion tests at room temperature and normal pressure. Figure 5.9(a) shows that serious localized corrosion occurred on the surface of the Ni-P coating after a 15-day immersion, and that the diameter of pits was in the micro-scale region. Figure 5.9(b) shows the pit surrounded by loose corrosion product.

In contrast, there was no evident localized corrosion on the surface of the Ni-P-Fe_3O_4 coating as shown in Figure 5.9(c) and almost the whole area was covered by corrosion product. The two coatings' morphologies differ because corrosion types differ. With structural defects within the coating, the surface of the Ni-P coating was more prone to local corrosion. However, the existence of Fe_3O_4 nanoparticles weakened the harmful impact of defects on the anti-corrosion property of the coating, thereby resulting in general corrosion. Because pitting corrosion on the Ni-P coating surface was more severe, the comparison of different coatings' morphologies confirmed that the Ni-P-Fe_3O_4 coating had better corrosion resistance.

5.2.4.2 Capsule test

After a high temperature, high-pressure corrosion test for 240 hours, the surfaces of the Ni-P coating and Ni-P-Fe_3O_4 coating were observed using OSM (Figure 5.10). Figure 5.10 shows that after the 10-day corrosion, there was obvious localized corrosion on the surface of the Ni-P coating. The corrosion product deposited around the pit. However, the surface of the Ni-P-Fe_3O_4 coating was still smooth without any corrosion product, and no significant corrosion sites could be found. This indicates a better corrosion resistance in a long-term test. With nanoscale sizes, nanoparticles filled the defects of the Ni-P coating, which worked as a protective barrier between the substrate and corrosion media. As localized corrosion is likely to occur in defects, incorporating nanoparticles can improve the stability of nanocomposite coating.

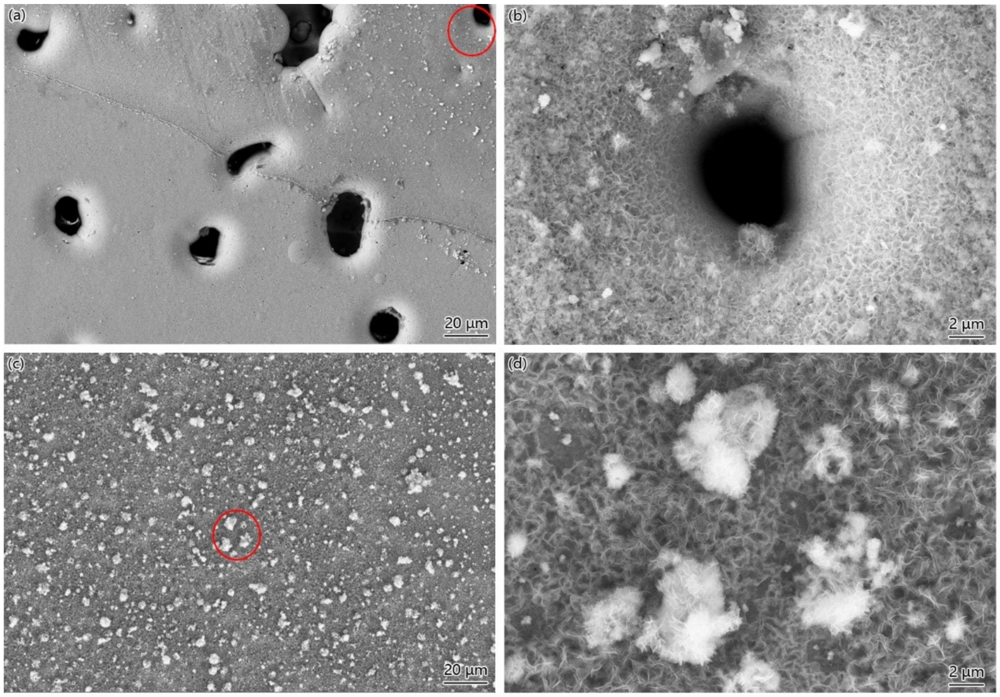

Figure 5.9 SEM morphologies of coatings after immersion for 360 h (a) Ni-P coating, (b) higher magnified image of Ni-P coating, (c) Ni-P-Fe_3O_4 (0.8 g/L) coating, (d) higher magnified image of Ni-P-Fe_3O_4 (0.8 g/L) coating.

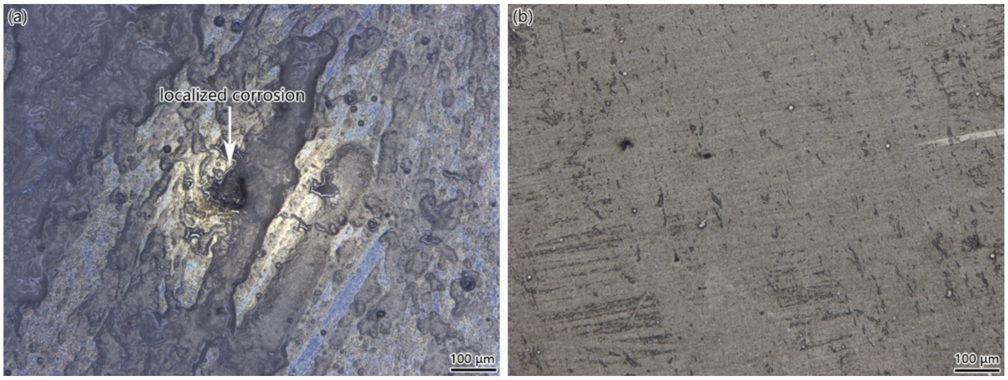

Figure 5.10 OSM morphologies of (a) Ni-P, and (b) Ni-P-Fe_3O_4 (0.8 g/L) coatings after high temperature, high-pressure corrosion test.

5.2.4.3 Autoclave test

The corrosion rate during the autoclave test can be determined by the weight loss of samples as follows:

$$V = \frac{8.76 \times 10^4 \, \Delta m}{S \, \rho t} \qquad (5\text{-}1)$$

Where V is the corrosion rate, mm/y; Δm is the mass loss, g; S is the exposure area of the specimen, cm^2; ρ is the density of the specimen, g/cm^3; and t is the corrosion time, h. As depicted in Figure 5.11, the corrosion rates of the Ni-P coatings and Ni-P-Fe_3O_4 (0.8 g/L) coatings after high temperature, high pressure corrosion tests were calculated using the weight loss method. The corrosion rate of the Ni-P coatings was 0.01661 mm/y, while that of the Ni-P-Fe_3O_4 coatings was 0.00668 mm/y, confirming that incorporating Fe_3O_4 nanoparticles can further improve the stability of the Ni-P coating.

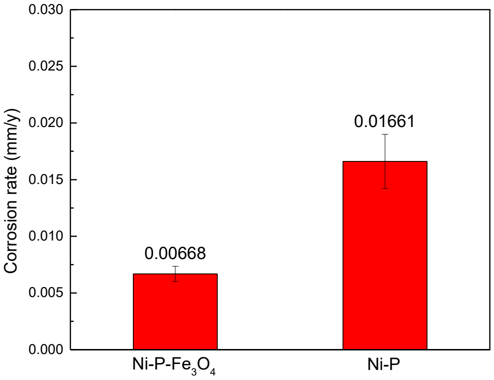

Figure 5.11 Corrosion rate of Ni-P and Ni-P-Fe_3O_4 (0.8 g/L) coatings during the high-temperature high-pressure corrosion process.

The corrosion product on the surfaces and morphologies of the coatings was also characterized by SEM, as shown in Figure 5.12. Apparently, loose corrosion product was uniformly distributed on the whole surface of the Ni-P coating, and no obvious nodular structures could be detected. This was due to the dissolution of the Ni-P coating during the general corrosion process. Nevertheless, nodular structures still existed on the Ni-P-Fe_3O_4 coating surface, and corrosion product covered only a small part of the Ni-P-Fe_3O_4 coating surface; it was especially concentrated at the boundary of nodular structures. It can be concluded that the Ni-P-Fe_3O_4 coating suffered less damage from corrosion, indicating better anti-corrosion properties and corresponding to results that had been calculated in electrochemical tests.

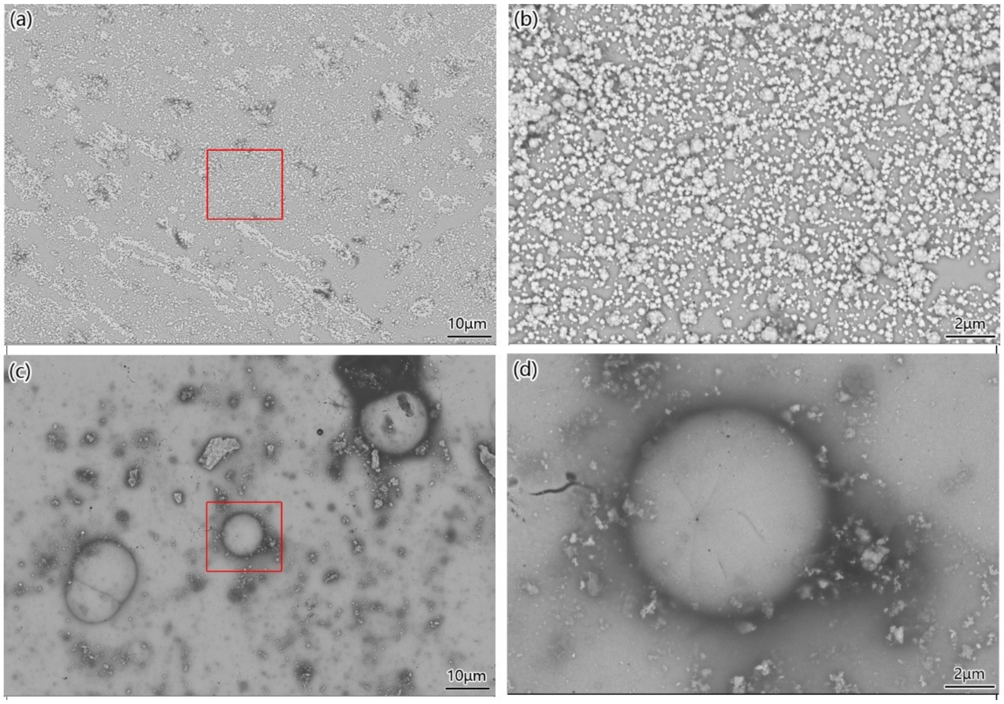

Figure 5.12 SEM morphologies of coatings after high-temperature high-pressure corrosion test for 200 h (a) Ni-P coating, (b) higher magnified image of Ni-P coating, (c) Ni-P-Fe_3O_4

(0.8 g/L) coating, (d) higher magnified image of Ni-P-Fe_3O_4 (0.8 g/L) coating.

5.2.5 Discussions

There are several possible explanations for the observed results. Electroless Ni-P coating works as a barrier film, protecting the weak substrate from meeting the corrosive media. The literature reports about Ni-P coatings suggest that nickel in the coating is likely to dissolve at OCP when the coating is immersed in the corrosive environment, enriching the phosphorus on the surface [48]. This sacrificing property leads to the formation of a layer with adsorbed hypophosphite anions. The layer will play an important role in blocking the water supply to the surface, preventing the nickel from dissolving. However, with the existence of the pores or small defects within the coatings, the corrosion process can still occur from the coating surface to the substrate. The nodule boundaries formed in the deposition process of Ni-P coating also act as main corrosion paths when the coating surface contacts corrosive media.

From surface morphology of Ni-P-0.8 g/L Fe_3O_4 coating, the density of pores is significantly reduced by co-depostion of nanoparticles. This is because incorporated nanoparticles can fill a part of pores, producing a more compact coating. It should be noted that the particles can also improve the coating thickness and reduce the nodule sizes by blocking the nodule boundaries, because the particles work as nucleation points during the growth of the coating.

When the concentration of nanoparticles was below a certain level (0.8 g/L), incorporating the Fe_3O_4 nanoparticles with the Ni-P coating helped to reduce porosity along with nodule sizes, and increase coating thickness. The Fe_3O_4 nanoparticles filled the pores and blocked nodule boundaries, acting as protective barriers against the initiation and aggravation of defect corrosion. In this concentration range (0-0.8 g/L), the corrosion resistance was enhanced as the nanoparticle concentration increased. However, when this concentration was higher than 0.8 g/L, the increased concentration led to an agglomeration of nanoparticles, creating a detrimental impact on the uniformity of coating surfaces and generating a loose surface. Poor uniformity enhanced the contact area between the surface layer and corrosion media, accelerating the corrosion processes [68,105]. Excessive nanoparticles deposited in the coating also decreased the phosphorus content, which was essential to the corrosion resistance.

5.3 Conclusions

1. Adding different amounts of Fe_3O_4 had a significant influence on the morphology of coatings. The co-deposition of Fe_3O_4 could decrease porosity. When the Fe_3O_4 concentration was under 0.8g/L, the coating surface was smooth with uniformly distributed Fe_3O_4. The Ni-P-Fe_3O_4 (0.8 g/L) coating had the lowest porosity. With a higher Fe_3O_4 concentration, large overlapping spherical, globular structures appeared, leading to a rougher surface. The structure of the coating was not changed by the Fe_3O_4. Both the Ni-P and Ni-P-Fe_3O_4 coatings were amorphous.

2. The thickness of the coatings was also highly affected by different nanoparticle concentrations. The appropriate addition of nanoparticles could enhance the thickness of the coating, while a higher level of concentration decreased the thickness.

3. All of the Ni-P-Fe_3O_4 coatings with varying concentrations of Fe_3O_4 nanoparticles showed a better corrosion resistance than the Ni-P coating. The critical level of nanoparticle concentrations for the Ni-P-Fe_3O_4 coating was 0.8 g/L, beyond which the nanoparticles would agglomerate and negatively affect the coatings' anti-corrosion properties. For corrosion resistance, the optimized concentration of Fe_3O_4 was 0.8 g/L.

4. Long-term corrosion tests also confirmed that the Ni-P-Fe_3O_4 coatings were more stable.

6. Conclusions

In this thesis, two kinds of Ni-P nanocomposite coatings were prepared and investigated.

1. Both the Ni-P-WC and Ni-P-Fe_3O_4 coatings exhibited a higher corrosion resistance than the Ni-P coating.

2. Immersion tests also confirmed that the Ni-P-WC and Ni-P-Fe_3O_4 coatings were more stable.

3. The crystal structure was not changed by the addition of nanoparticles.

4. Incorporating WC nanoparticles enhanced the Ni-P coating's microhardness. Heat treatment can further improve this beneficial effect.

5. The concentration of nanoparticles in the plating bath significantly influenced the coatings' properties. There is a critical level below which adding nanoparticles improved the coatings' properties (e.g., thickness, compactness, microhardness, anti-corrosion ability). However, excessive nanoparticle concentrations resulted in an agglomeration of nanoparticles, which was detrimental to the performance of the Ni-P nanocomposite coatings.

7. Future work

Optimization

Only the effect of the nanoparticle concentration was studied in this thesis; some other significant factors such as plating temperature, surfactant concentration, rotating speed, and pre-treatments can also play important roles in coating properties. Therefore, it is essential to further modify the coating via various methods.

Corrosion mechanism

In this thesis, corrosion tests were conducted in the presence of H_2S and CO_2 at room temperature under the normal pressure, and only CO_2 was injected into the autoclave in high-temperature and high-pressure tests. However, real-life conditions involve a combination of high temperature, high pressure, and the coexistence of H_2S and CO_2. Therefore, it is important to test the anti-corrosion properties of Ni-P coating and Ni-P nanocomposite coatings in high-temperature, high-pressure tests with H_2S and CO_2 to simulate the real environment in the oil field and study coating's failure mechanism. Such tests will clarify the relationships between the partial pressure of H_2S and CO_2, temperature, the concentration of brine, and corrosion resistance.

The investigation of localized corrosion and initiation of pits through STM

Localized corrosion is the most common form occurring on the surface of carbon steel in oil fields. This kind of corrosion is likely to be induced by structural defects in the material. Although

Ni-P nanocomposite coatings have desirable properties, defects exist in their structures. Understanding the initial stage of localized corrosion enables researchers to design better coatings and prevent corrosion. Scanning Tunneling Microscopy (STM) is an in situ, non-destructive form of measurement that can be used to investigate local corrosion events on the coating surface. A core component of STM is the microprobe, which can be precisely positioned to the region of interest on the surface. SEM can generate potential/current mappings over a specimen surface and topographical images, leading to a better understanding of the initiation and propagation of localized corrosion around the defects and establishing the relationship between localized corrosion events and the morphology change.

References

[1] Rui, Z., Wang, X., Zhang, Z., Lu, J., Chen, G., Zhou, X., & Patil, S. (2018). A realistic and integrated model for evaluating oil sands development with steam assisted gravity drainage technology in Canada. *Applied Energy, 213*, 76-91.

[2] Roth, E., Bank, T., Howard, B., & Granite, E. (2017). Rare Earth Elements in Alberta Oil Sand Process Streams. *Energy & Fuels, 31*(5), 4714-4720.

[3] Popoola, L. T., Grema, A. S., Latinwo, G. K., Gutti, B., & Balogun, A. S. (2013). Corrosion problems during oil and gas production and its mitigation. *International Journal of Industrial Chemistry, 4*(1), 35.

[4] Mansor, N. I. I., Abdullah, S., Ariffin, A. K., & Syarif, J. (2014). A review of the fatigue failure mechanism of metallic materials under a corroded environment. *Engineering Failure Analysis, 42*, 353-365.

[5] Hallman, T., Yung, V. Y. B., & Albertson, A. (2015, April). Analysis of Wellbore Failures and Re-Design of Slotted Liners for Horizontal Wells Applied in a Heavy Oilfield. In *SPE Western Regional Meeting*. Society of Petroleum Engineers.

[6] Yang, S., Li, X., Renevier, N. M., & Teer, D. G. (2001). Tribological properties and wear mechanism of sputtered C/Cr coating. *Surface and Coatings Technology, 142*, 85-93.

[7] Hosking, N. C., Ström, M. A., Shipway, P. H., & Rudd, C. D. (2007). Corrosion resistance of zinc-magnesium coated steel. *Corrosion science, 49*(9), 3669-3695.

[8] Volovitch, P., Vu, T. N., Allély, C., Aal, A. A., & Ogle, K. (2011). Understanding corrosion via corrosion product characterization: II. Role of alloying elements in improving the corrosion resistance of Zn-Al-Mg coatings on steel. *Corrosion Science, 53*(8), 2437-2445.

[9] PalDey, S. C. D. S., & Deevi, S. C. (2003). Single layer and multilayer wear resistant coatings of (Ti, Al) N: a review. *Materials Science and Engineering: A, 342*(1), 58-79.

[10] Toma, D., Brandl, W., & Marginean, G. (2001). Wear and corrosion behaviour of thermally sprayed cermet coatings. *Surface and Coatings Technology, 138*(2), 149-158.

[11] Chen, X. H., Chen, C. S., Xiao, H. N., Cheng, F. Q., Zhang, G., & Yi, G. J. (2005). Corrosion

behavior of carbon nanotubes-Ni composite coating. *Surface and Coatings Technology, 191*(2), 351-356.

[12] Elansezhian, R., Ramamoorthy, B., & Nair, P. K. (2008). Effect of surfactants on the mechanical properties of electroless (Ni-P) coating. *Surface and Coatings Technology, 203*(5), 709-712.

[13] Ranganatha, S., Venkatesha, T. V., & Vathsala, K. (2012). Process and properties of electroless Ni-Cu-P-ZrO_2 nanocomposite coatings. *Materials Research Bulletin, 47*(3), 635-645.

[14] Ranganatha, S., Venkatesha, T. V., & Vathsala, K. (2010). Development of electroless Ni-Zn-P/nano-TiO_2 composite coatings and their properties. *Applied Surface Science, 256*(24), 7377-7383.

[15] Narayanan, T. S., Krishnaveni, K., & Seshadri, S. K. (2003). Electroless Ni-P/Ni-B duplex coatings: preparation and evaluation of microhardness, wear and corrosion resistance. *Materials Chemistry and Physics, 82*(3), 771-779.

[16] Li, G., Tang, J., & Sheng, J. (2007). Preparation and electrocatalytic property of WC/carbon nanotube composite. *Electrochimica acta, 52*(5), 2018-2023.

[17] Zhao, C., & Yao, Y. (2014). Preparation and Mechanical Properties of Electroless Nickel-Phosphorus-Tungsten Carbide Nanocomposite Coatings. J*ournal of materials engineering and performance, 23*(1), 193-197.

[18] Chu, Y., Fan, C., Zhang, Q., Zan, C., Ma, D., Jiang, H., ... & Wei, F. (2014). The oxidation of heavy oil to enhance oil recovery: The numerical model and the criteria to describe the low and high temperature oxidation. *Chemical Engineering Journal, 248*, 422-429.

[19] Muraza, O., & Galadima, A. (2015). Aquathermolysis of heavy oil: A review and perspective on catalyst development. *Fuel, 157*, 219-231.

[20] Case, R., Mahajanam, S., Dunn, J., Joosten, M., Achour, M., Marchebois, H., & Bonis, M. (2014). High Temperature Corrosion Studies in Simulated SAGD Produced Fluids. *Corrosion, 71*(4), 536-545.

[21] Whittaker, J., Liu, Q., Brown, D. J., & Marsden, R. (2014, May). Corrosion management and mechanism study on SAGD Brackish water system. In *CORROSION 2014*. NACE International.

[22] Dugstad, A., Clausen, S., & Morland, B. (2011, January). Transport of dense phase CO_2 in C-steel pipelines-when is corrosion an issue. In *CORROSION 2011*. NACE International.

[23] Pehlke, T. (2017). *Studies of Aqueous Hydrogen Sulfide Corrosion in Producing SAGD Wells* (Doctoral dissertation, University of Calgary).

[24] Yu, B., Li, D. Y., & Grondin, A. (2013). Effects of the dissolved oxygen and slurry velocity on erosion-corrosion of carbon steel in aqueous slurries with carbon dioxide and silica sand. *Wear, 302*(1), 1609-1614.

[25] Liu, Q., Whittaker, J., & Marsden, R. (2015, May). Mystery of SAGD Casing Gas Corrosivity and Corrosion Mitigation Strategy. In *CORROSION 2015*. NACE International.

[26] Liu, Q. Y., Mao, L. J., & Zhou, S. W. (2014). Effects of chloride content on CO_2 corrosion of carbon steel in simulated oil and gas well environments. *Corrosion Science, 84*, 165-171.

[27] Li, W., & Li, D. Y. (2005). Variations of work function and corrosion behaviors of deformed copper surfaces. *Applied Surface Science, 240*(1), 388-395.

[28] Sun, W., Pugh, D. V., Ling, S., Reddy, R. V., Pacheco, J. L., Nisbet, R. S., ... & Morshidi, L. (2011, January). Understanding and quantifying corrosion of L80 carbon steel in sour environments. In *CORROSION 2011*. NACE International.

[29] Kermani, M. B., & Morshed, A. (2003). Carbon dioxide corrosion in oil and gas production-a compendium. *Corrosion, 59*(8), 659-683.

[30] Islam, M. A., & Farhat, Z. N. (2015). Characterization of the Corrosion Layer on Pipeline Steel in Sweet Environment. *Journal of Materials Engineering and Performance, 24*(8), 3142-3158.

[31] Dugstad, A. (2006, January). Fundamental aspects of CO_2 metal loss corrosion-part 1: mechanism. In *CORROSION 2006*. NACE International.

[32] Sun, Y., & Nesic, S. (2004). A parametric study and modeling on localized CO_2 corrosion in horizontal wet gas flow. *CORROSION 2004*.

[33] Crolet, J. L., Thevenot, N., & Nesic, S. (1998). Role of conductive corrosion products in the protectiveness of corrosion layers. *Corrosion, 54*(3), 194-203.

[34] Bai, P., Zheng, S., Zhao, H., Ding, Y., Wu, J., & Chen, C. (2014). Investigations of the diverse corrosion products on steel in a hydrogen sulfide environment. *Corrosion Science, 87*, 397-406.

[35] Zheng, Y., Brown, B., & Nešić, S. (2013). Electrochemical study and modeling of H_2S corrosion of mild steel. *Corrosion, 70*(4), 351-365.

[36] Lucio-Garcia, M. A., Gonzalez-Rodriguez, J. G., Casales, M., Martinez, L., Chacon-Nava, J. G., Neri-Flores, M. A., & Martinez-Villafañe, A. (2009). Effect of heat treatment on H_2S corrosion of a micro-alloyed C-Mn steel. *Corrosion Science, 51*(10), 2380-2386.

[37] Bai, P., Zhao, H., Zheng, S., & Chen, C. (2015). Initiation and developmental stages of steel corrosion in wet H_2S environments. *Corrosion Science, 93*, 109-119.

[38] Guan, S. W., Gritis, N., Jackson, A., & Singh, P. (2005). Advanced onshore and offshore pipeline coating technologies.

[39] Hsu, C. I., Wang, G. L., Ger, M. D., & Hou, K. H. (2016). Corrosion Behaviour of Electroless Deposited Ni-P/BN (h) Composite Coating. *INTERNATIONAL JOURNAL OF ELECTROCHEMICAL SCIENCE, 11*(6), 4352-4361.

[40] Ma, J., Fuss, T., & Shi, J. (2016, February). Iron Sulfide Scale Deposition in Deep Sour Reservoirs. In *SPE International Conference and Exhibition on Formation Damage Control*. Society of Petroleum Engineers.

[41] Kharshan, M., & Furman, A. (1998, December). Incorporating Vapor Corrosion Inhibitors (VCIS) in Oil and Gas Pipeline Additive Formulations. In *CORROSION-NATIONAL ASSOCIATION OF CORROSION ENGINEERS ANNUAL CONFERENCE*. NACE.

[42] Pedeferri, P. (1996). Cathodic protection and cathodic prevention. *Construction and building materials, 10*(5), 391-402.

[43] Krishnan, K. H., John, S., Srinivasan, K. N., Praveen, J., Ganesan, M., & Kavimani, P. M. (2006). An overall aspect of electroless Ni-P depositions-a review article. *Metallurgical and Materials Transactions A, 37*(6), 1917-1926.

[44] Agarwala, R. C., & Agarwala, V. (2003). Electroless alloy/composite coatings: A review. *Sadhana, 28*(3-4), 475-493.

[45] Kundu, S., Das, S. K., & Sahoo, P. (2014). Properties of electroless nickel at elevated

temperature-a review. *Procedia Engineering, 97*, 1698-1706.

[46] Guo, Z., Keong, K. G., & Sha, W. (2003). Crystallisation and phase transformation behaviour of electroless nickel phosphorus platings during continuous heating. *Journal of Alloys and Compounds, 358*(1), 112-119.

[47] Sudagar, J., Lian, J., & Sha, W. (2013). Electroless nickel, alloy, composite and nano coatings–A critical review. *Journal of Alloys and Compounds, 571*, 183-204.

[48] Ashassi-Sorkhabi, H., & Rafizadeh, S. H. (2004). Effect of coating time and heat treatment on structures and corrosion characteristics of electroless Ni-P alloy deposits. *Surface and coatings Technology, 176*(3), 318-326.

[49] Hubbell, F. N. (1978). Chemically Deposited Composites-A New Generation of Electroless Coatings. *Transactions of the IMF, 56*(1), 65-69.

[50] Xu, H., Yang, Z., Li, M. K., Shi, Y. L., Huang, Y., & Li, H. L. (2005). Synthesis and properties of electroless Ni-P-Nanometer Diamond composite coatings. *Surface and coatings technology, 191*(2), 161-165.

[51] Ma, C., Wu, F., Ning, Y., Xia, F., & Liu, Y. (2014). Effect of heat treatment on structures and corrosion characteristics of electroless Ni-P-SiC nanocomposite coatings. *Ceramics International, 40*(7), 9279-9284.

[52] Karthikeyan, S., & Ramamoorthy, B. (2014). Effect of reducing agent and nano Al_2O_3 particles on the properties of electroless Ni-P coating. *Applied Surface Science, 307*, 654-660.

[53] Islam, M., Azhar, M. R., Fredj, N., Burleigh, T. D., Oloyede, O. R., Almajid, A. A., & Shah, S. I. (2015). Influence of SiO_2 nanoparticles on hardness and corrosion resistance of electroless Ni-P coatings. *Surface and Coatings Technology, 261*, 141-148.

[54] Chen, W. X., Tu, J. P., Wang, L. Y., Gan, H. Y., Xu, Z. D., & Zhang, X. B. (2003). Tribological application of carbon nanotubes in a metal-based composite coating and composites. *Carbon, 41*(2), 215-222.

[55] Chen, W. X., Tu, J. P., Gan, H. Y., Xu, Z. D., Wang, Q. G., Lee, J. Y., ... & Zhang, X. B. (2002). Electroless preparation and tribological properties of Ni-P-Carbon nanotube composite coatings under lubricated condition. *Surface and Coatings Technology, 160*(1), 68-73.

[56] Reddy, V. V. N., Ramamoorthy, B., & Nair, P. K. (2000). A study on the wear resistance of electroless Ni-P/Diamond composite coatings. *Wear, 239*(1), 111-116.

[57] Sarret, M., Müller, C., & Amell, A. (2006). Electroless NiP micro-and nano-composite coatings. *Surface and Coatings Technology, 201*(1), 389-395.

[58] Sheela, G., & Pushpavanam, M. (2002). Diamond-dispersed electroless nickel coatings. *Metal finishing, 100*(1), 45-47.

[59] Zarebidaki, A., & Allahkaram, S. R. (2011). Effect of surfactant on the fabrication and characterization of Ni-P-CNT composite coatings. *Journal of Alloys and Compounds, 509*(5), 1836-1840.

[60] Ashassi-Sorkhabi, H., & Es, M. (2013). Corrosion resistance enhancement of electroless Ni-P coating by incorporation of ultrasonically dispersed diamond nanoparticles. *Corrosion Science, 77*, 185-193.

[61] Hamid, Z. A., & Elkhair, M. A. (2002). Development of electroless nickel-phosphorous composite deposits for wear resistance of 6061 aluminum alloy. *Materials Letters, 57*(3), 720-726.

[62] Aal, A. A., Hassan, H. B., & Rahim, M. A. (2008). Nanostructured Ni-P-TiO_2 composite coatings for electrocatalytic oxidation of small organic molecules. *Journal of Electroanalytical Chemistry, 619*, 17-25.

[63] Rabizadeh, T., & Allahkaram, S. R. (2011). Corrosion resistance enhancement of Ni–P electroless coatings by incorporation of nano-SiO_2 particles. *Materials & Design, 32*(1), 133-138.

[64] Mafi, I. R., & Dehghanian, C. (2011). Studying the effects of the addition of TiN nanoparticles to Ni-P electroless coatings. *Applied Surface Science, 258*(5), 1876-1880.

[65] de Hazan, Y., Werner, D., Z'graggen, M., Groteklaes, M., & Graule, T. (2008). Homogeneous Ni-P/Al_2O_3 nanocomposite coatings from stable dispersions in electroless nickel baths. *Journal of colloid and interface science, 328*(1), 103-109.

[66] Sadreddini, S., Salehi, Z., & Rassaie, H. (2015). Characterization of Ni-P-SiO 2 nano-composite coating on magnesium. *Applied Surface Science, 324*, 393-398.

[67] Ardakani, S. R., Afshar, A., Sadreddini, S., & Ghanbari, A. A. (2017). Characterization of Ni-P-SiO_2-Al_2O_3 nano-composite coatings on aluminum substrate. *Materials Chemistry and Physics,*

189, 207-214.

[68] Afroukhteh, S., Dehghanian, C., & Emamy, M. (2012). Preparation of electroless Ni-P composite coatings containing nano-scattered alumina in presence of polymeric surfactant. Progress in Natural Science: *Materials International, 22*(4), 318-325.

[69] Chen, W., Gao, W., & He, Y. (2010). A novel electroless plating of Ni-P-TiO_2 nano-composite coatings. *Surface and Coatings Technology, 204*(15), 2493-2498.

[70] Luo, H., Leitch, M., Behnamian, Y., Ma, Y., Zeng, H., & Luo, J. L. (2015). Development of electroless Ni-P/nano-WC composite coatings and investigation on its properties. *Surface and Coatings Technology, 277*, 99-106.

[71] Heakal, F. E. T., & Maanoum, M. A. (2016). Role of Some Plating Parameters in the Properties of Ni-P/Al_2O_3 Nanocomposite Coatings on Mg alloy. *Int. J. Electrochem. Sci, 11*, 7198-7215.

[72] Soleimani, R., Mahboubi, F., Arman, S. Y., Kazemi, M., & Maniee, A. (2015). Development of mathematical model to evaluate microstructure and corrosion behavior of electroless Ni-P/nano-SiC coating deposited on 6061 aluminum alloy. *Journal of Industrial and Engineering Chemistry, 23*, 328-337.

[73] Bigdeli, F., & Allahkaram, S. R. (2009). An investigation on corrosion resistance of as-applied and heat treated Ni-P/nanoSiC coatings. *Materials & Design, 30*(10), 4450-4453.

[74] Sharma, S., Sharma, S., Sharma, A., & Agarwala, V. (2016). Co-deposition of Synthesized ZnO Nanoparticles into Ni-P Matrix Using Electroless Technique and Their Corrosion Study. *Journal of Materials Engineering and Performance, 25*(10), 4383-4393.

[75] Momenzadeh, M., & Sanjabi, S. (2012). The effect of TiO2 nanoparticle codeposition on microstructure and corrosion resistance of electroless Ni-P coating. *Materials and Corrosion, 63*(7), 614-619.

[76] Huan, Z., Scarmozzino, R., Nagy, G., Steel, J., & Osgood, R. M. (2000). Realization of a compact and single-mode optical passive polarization converter. *IEEE Photonics Technology Letters, 12*(3), 317-319.

[77] Yadav, D. K., Chauhan, D. S., Ahamad, I., & Quraishi, M. A. (2013). Electrochemical behavior of steel/acid interface: adsorption and inhibition effect of oligomeric aniline. *RSC Advances, 3*(2), 632-646.

[78] Fattah-Alhosseini, A., Mosavi, M., & Allahdadi, A. (2011). An Electrochemical Impedance Study of AISI 321 Stainless Steel in 0.5 M H_2SO_4. *International Journal of Electrochemistry*, 2011.

[79] Liu, J., Wang, X., Tian, Z., Yuan, M., & Ma, X. (2015). Effect of copper content on the properties of electroless Ni-Cu-P coatings prepared on magnesium alloys. *Applied Surface Science, 356*, 289-293.

[80] Mansfeld, F. (1990). Electrochemical impedance spectroscopy (EIS) as a new tool for investigating methods of corrosion protection. *Electrochimica Acta*, *35*(10), 1533-1544.

[81] Goldstein, J. I., Newbury, D. E., Michael, J. R., Ritchie, N. W., Scott, J. H. J., & Joy, D. C. (2003). *Scanning electron microscopy and X-ray microanalysis*. Springer.

[82] Agarwala, R. C., Agarwala, V., & Sharma, R. (2006). Electroless Ni-P Based Nanocoating Technology-A Review. *Synthesis and Reactivity in Inorganic, Metal-Organic and Nano-Metal Chemistry, 36*(6), 493-515.

[83] Liu, G., Huang, Z., Wang, L., Sun, W., Wang, S., & Deng, X. (2013). Effects of Ce^{4+} on the structure and corrosion resistance of electroless deposited Ni-Cu-P coating. *Surface and Coatings Technology, 222*, 25-30.

[84] Chen, M. A., Cheng, N., Ou, Y. C., & Li, J. M. (2013). Corrosion performance of electroless Ni-P on polymer coating of MAO coated AZ31 magnesium alloy. *Surface and Coatings Technology, 232*, 726-733.

[85] Allahkaram, S. R., Nazari, M. H., Mamaghani, S., & Zarebidaki, A. (2011). Characterization and corrosion behavior of electroless Ni–P/nano-SiC coating inside the CO_2 containing media in the presence of acetic acid. *Materials & Design, 32*(2), 750-755.

[86] Dong, D., Chen, X. H., Xiao, W. T., Yang, G. B., & Zhang, P. Y. (2009). Preparation and properties of electroless Ni-P-SiO_2 composite coatings. *Applied Surface Science, 255*(15), 7051-7055.

[87] Xu, R., Wang, J., He, L., & Guo, Z. (2008). Study on the characteristics of Ni-W-P composite coatings containing nano-SiO_2 and nano-CeO_2 particles. *Surface and Coatings Technology, 202*(8), 1574-1579.

[88] Pfeiffer, H., Tancret, F., & Brousse, T. (2005). Synthesis, characterization and thermal stability

of Ni_3P coatings on nickel. *Materials chemistry and physics, 92*(2), 534-539.

[89] Balaraju, J. N., & Rajam, K. S. (2006). Influence of particle size on the microstructure, hardness and corrosion resistance of electroless Ni-P-Al_2O_3 composite coatings. *Surface and Coatings Technology, 200*(12), 3933-3941.

[90] Palaniappa, M., & Seshadri, S. K. (2007). Structural and phase transformation behaviour of electroless Ni-P and Ni-W-P deposits. *Materials Science and Engineering: A, 460*, 638-644.

[91] Sun, S., Liu, J., Yan, C., & Wang, F. (2008). A novel process for electroless nickel plating on anodized magnesium alloy. *Applied Surface Science, 254*(16), 5016-5022.

[92] Balaraju, J. N., & Rajam, K. S. (2007). Electroless deposition and characterization of high phosphorus13; Ni-P-Si_3N_4 composite coatings. *International Journal of Electrochemical Science, 2*(10), 747-761.

[93] Balaraju, J. N., Selvi, V. E., & Rajam, K. S. (2010). Electrochemical behavior of low phosphorus electroless Ni-P-Si_3N_4 composite coatings. *Materials Chemistry and Physics, 120*(2), 546-551.

[94] Rahimi, A. R., Modarress, H., & Amjad Iranagh, S. (2011). Effect of alumina nanoparticles as nanocomposites on morphology and corrosion resistance of electroless Ni-P coatings. *Surface Engineering, 27*(1), 26-31.

[95] Ebrahimian-Hosseinabadi, M., Azari-Dorcheh, K., & Vaghefi, S. M. (2006). Wear behavior of electroless Ni-P-B_4C composite coatings. *Wear, 260*(1), 123-127.

[96] Li, Z., Wang, J., Lu, J., & Meng, J. (2013). Tribological characteristics of electroless Ni-P-MoS_2 composite coatings at elevated temperatures. *Applied Surface Science, 264*, 516-521.

[97] Sivandipoor, I., & Ashrafizadeh, F. (2012). Synthesis and tribological behaviour of electroless Ni-P-WS_2 composite coatings. *Applied Surface Science, 263*, 314-319.

[98] Kolen'ko, Y. V., Bañobre-López, M., Rodríguez-Abreu, C., Carbó-Argibay, E., Sailsman, A., Piñeiro-Redondo, Y., ... & Rivas, J. (2014). Large-scale synthesis of colloidal Fe_3O_4 nanoparticles exhibiting high heating efficiency in magnetic hyperthermia. *The Journal of Physical Chemistry C, 118*(16), 8691-8701.

[99] Tian, Q., Wang, Q., Yao, K. X., Teng, B., Zhang, J., Yang, S., & Han, Y. (2014).

Multifunctional Polypyrrole@ Fe_3O_4 Nanoparticles for Dual-Modal Imaging and In Vivo Photothermal Cancer Therapy. *Small, 10*(6), 1063-1068.

[100] He, C., Wu, S., Zhao, N., Shi, C., Liu, E., & Li, J. (2013). Carbon-encapsulated Fe_3O_4 nanoparticles as a high-rate lithium ion battery anode material. *ACS nano, 7*(5), 4459-4469.

[101] Wu, Z. S., Yang, S., Sun, Y., Parvez, K., Feng, X., & Müllen, K. (2012). 3D nitrogen-doped graphene aerogel-supported Fe3O4 nanoparticles as efficient electrocatalysts for the oxygen reduction reaction. *Journal of the American Chemical Society, 134*(22), 9082-9085.

[102] Sadreddini, S., Ardakani, S. R., & Rassaee, H. (2017). Corrosion Behavior and Microhardness of Ni-P-SiO_2-Al_2O_3 Nano-composite Coatings on Magnesium Alloy. *Journal of Materials Engineering and Performance, 26*(5), 2032-2039.

[103] Sharma, A., & Singh, A. K. (2013). Electroless Ni-P and Ni-P-Al_2O_3 nanocomposite coatings and their corrosion and wear resistance. *Journal of materials engineering and performance, 22*(1), 176-183.

[104] Luo, H., Wang, X., Gao, S., Dong, C., & Li, X. (2017). Synthesis of a duplex Ni-P-YSZ/Ni-P nanocomposite coating and investigation of its performance. *Surface and Coatings Technology, 311*, 70-79.

[105] Sadreddini, S., & Afshar, A. (2014). Corrosion resistance enhancement of Ni-P-nano SiO_2 composite coatings on aluminum. *Applied Surface Science, 303*, 125-130.